Monthly Notices of the ROYAL ASTRONOMICAL SOCIETY

MNRAS **519,** 931–947 (2023) https://doi.org/10.1093/mnras/stac3497
Advance Access publication 2022 November 30

MUSE-ALMA Haloes – VIII. Statistical study of circumgalactic medium gas

S. Weng [1,2,3,4]★ C. Péroux [1,5] A. Karki,[6] R. Augustin [7] V. P. Kulkarni,[6] R. Szakacs,[1] M. A. Zwaan,[1] A. Klitsch [8] A. Hamanowicz [7] E. M. Sadler [2,3,4] A. Biggs [1] A. Y. Fresco,[9] M. Hayes [10] J. C. Howk,[11] G. G. Kacprzak [12,3] H. Kuntschner,[1] D. Nelson [13] and M. Pettini[14]

[1]*European Southern Observatory, Karl-Schwarzschildstrasse 2, D-85748 Garching bei München, Germany*
[2]*Sydney Institute for Astronomy, School of Physics A28, University of Sydney, NSW 2006, Australia*
[3]*ARC Centre of Excellence for All Sky Astrophysics in 3 Dimensions (ASTRO 3D) , Canberra, Australian Capital Territory 2611, Australia*
[4]*ATNF, CSIRO Space and Astronomy, PO Box 76, Epping, NSW 1710, Australia*
[5]*Aix Marseille Université, CNRS, LAM (Laboratoire d'Astrophysique de Marseille) UMR 7326, F-13388 Marseille, France*
[6]*Department of Physics and Astronomy, University of South Carolina, Columbia, SC 29208, USA*
[7]*Space Telescope Science Institute, 3700 San Martin Drive, Baltimore, MD 21218, USA*
[8]*DARK, Niels Bohr Institute, University of Copenhagen, Jagtvej 128, DK-2200 Copenhagen, Denmark*
[9]*Max-Planck-Institut für Extraterrestrische Physik (MPE), Giessenbachstrasse 1, D-85748 Garching, Germany*
[10]*Stockholm University, Department of Astronomy and Oskar Klein Centre for Cosmoparticle Physics, AlbaNova University Centre, SE-10691 Stockholm, Sweden*
[11]*Department of Physics, University of Notre Dame, Notre Dame, IN 46556, USA*
[12]*Centre for Astrophysics and Supercomputing, Swinburne University of Technology, Hawthorn, Victoria 3122, Australia*
[13]*Universität Heidelberg, Zentrum für Astronomie, Institut für theoretische Astrophysik, Albert-Ueberle-Str 2, D-69120 Heidelberg, Germany*
[14]*Institute of Astronomy, University of Cambridge, Madingley Road, Cambridge CB3 0HA, UK*

Accepted 2022 November 20. Received 2022 November 20; in original form 2022 August 30

ABSTRACT

The distribution of gas and metals in the circumgalactic medium (CGM) plays a critical role in how galaxies evolve. The MUSE-ALMA Haloes survey combines MUSE, ALMA, and HST observations to constrain the properties of the multiphase gas in the CGM and the galaxies associated with the gas probed in absorption. In this paper, we analyse the properties of galaxies associated with 32 strong H I Ly-α absorbers at redshift $0.2 \lesssim z \lesssim 1.4$. We detect 79 galaxies within ± 500 kms^{-1} of the absorbers in our 19 MUSE fields. These associated galaxies are found at physical distances from 5.7 kpc and reach star formation rates as low as 0.1 $M_\odot$ yr^{-1}. The significant number of associated galaxies allows us to map their physical distribution on the Δv and b plane. Building on previous studies, we examine the physical and nebular properties of these associated galaxies and find the following: (i) 27/32 absorbers have galaxy counterparts and more than 50 per cent of the absorbers have two or more associated galaxies, (ii) the H I column density of absorbers is anticorrelated with the impact parameter (scaled by virial radius) of the nearest galaxy as expected from simulations, (iii) the metallicity of associated galaxies is typically larger than the absorber metallicity, which decreases at larger impact parameters. It becomes clear that while strong H I absorbers are typically associated with more than a single galaxy, we can use them to statistically map the gas and metal distribution in the CGM.

Key words: galaxies: abundance – galaxies: evolution – galaxies: formation – galaxies: haloes – quasars: absorption lines.

1 INTRODUCTION

The circumgalactic medium (CGM) extends beyond a galaxy's disc and interstellar medium (ISM) to the intergalactic medium (IGM) and is the region where inflowing, outflowing, and recycled gas transits (Tumlinson, Peeples & Werk 2017). Inflowing metal-poor gas from dark matter filaments is expected to fuel star formation within galaxies, while galactic winds eject baryons into the halo or even the IGM at larger velocities. A portion of this wind material is expected to be recycled onto the galaxy in the form of galactic fountains (Fraternali 2017). The combination of these processes results in a continuous cycling of baryons within and outside galaxies, and dictates how galaxies evolve (Péroux & Howk 2020). Observationally linking the distribution of baryons in the CGM with galaxy properties is critical to constraining the role of the CGM in galaxy evolution.

Characterizing the distribution of matter in the CGM beyond the local Universe has been challenging because of the diffuse nature of material that comprises it. Despite the success of several studies probing the CGM in emission, the systems discovered so far contain powerful active galactic nuclei (AGN), starbursting galaxies or are highly overdense regions (e.g. Epinat et al. 2018; Johnson et al. 2018; Chen et al. 2019; Burchett et al. 2021; Cameron et al. 2021; Helton et al. 2021). Studies of systems more representative of 'average' galaxies and galaxy groups often require significant exposure times to obtain a detection in emission (Zabl et al. 2021; Leclercq et al.

★ E-mail: swen2649@uni.sydney.edu.au

2022) or stacking (Steidel et al. 2011; Momose et al. 2014; Chen et al. 2020b). While emission-line studies enable the spatial mapping of the CGM, absorption-line spectroscopy allows the CGM gas to be detected to much lower column densities. By observing the single sightlines towards bright background quasi-stellar objects, the column densities probed are only limited by the apparent brightness of the background source and reach far greater depths than what can be observed in emission. To remedy the fact that this technique only probes a single sightline through a galaxy's CGM, large samples are required to statistically map the distribution of baryons and place observational constraints that can inform simulations.

For over two decades, the identification of galaxies associated with absorbers in QSO spectra (e.g. Bergeron 1986a; Bergeron & Boissé 1991) required both imaging and spectroscopy. This was often inefficient as the targets selected for spectroscopic follow-up due to their proximity to the QSO were found to be not always at the absorber redshift. The advent of integral field spectroscopy (IFS) meant that associated galaxies could now be discovered in a more unbiased and efficient manner, and the sample of quasar-galaxy pairs has since increased in size by more than two orders of magnitude. In particular, the Multi-Unit Spectrographic Explorer (MUSE) instrument (Bacon et al. 2010), with its wide 1×1 arcmin field of view (FoV) and simultaneous wavelength coverage 4700–9350 Å, has led to a proliferation of surveys characterizing the CGM by studying galaxies in the vicinity of absorbers. The programs MusE GAs FLOw and Wind (MEGAFLOW; Schroetter et al. 2016a) and MUSE Analysis of Gas around Galaxies (Lofthouse et al. 2020) span redshift $0.2 \lesssim z \lesssim 4$ and probe gas in the CGM through various tracers such as Mg II ($\lambda\lambda$2795, 2803) and H I absorption. The MUSE Quasar-field Blind Emitters Survey (Muzahid et al. 2020) targets bright high-z QSOs with absorption lines to search for Lyman-α emitters at $z \approx 3.3$ in the field. The Keck Cosmic Web Imager (KCWI; Morrissey et al. 2018) integral field spectrograph with its bluer wavelength coverage has also been used for similar studies like the CGM at Cosmic Noon with KCWI program (Nielsen et al. 2020).

Amongst the possible absorption lines observed towards bright background QSOs, the Ly-α 1215 Å line is an important tracer of neutral hydrogen (H I), the fundamental building block of stars in galaxies. Several surveys have targeted Ly-α absorbers at an intermediate redshift range $0.4 \lesssim z \lesssim 2$, such as the Cosmic Ultraviolet Baryons Survey (CUBS; Chen et al. 2020a) and the Bimodal Absorption System Imaging Campaign (BASIC; Berg et al. 2022). The CUBS survey targeted 15 QSOs selected by their near ultraviolet brightness to search primarily for systems with column densities $\log[N(\mathrm{H\,I})/\mathrm{cm}^{-2}]<19.0$. Galaxies associated with these low column-density systems vary significantly in properties such as star formation rate (SFR), metallicity, and environment (Chen et al. 2020a; Cooper et al. 2021). Similarly, the BASIC survey targeted a sample of 36 Lyman limit systems (LLS) and pseudo-LLS absorbers at $z \lesssim 1$ and found no associated galaxies for the majority of absorbers with <10 per cent solar metallicity, pointing to a population of low-metallicity absorbers not associated with the CGM (Berg et al. 2022).

Tangential to these surveys is the MUSE-Atacama Large Millimetre/submillimetre Array (ALMA) Haloes Survey, where 32 H I Ly-α absorbers with column densities ranging from $18.1 \lesssim \log N(\mathrm{H\,I}) \lesssim 21.7$ at redshift $0.2 \lesssim z \lesssim 1.4$ are targeted (see Péroux et al. 2022 for an overview). The targets were selected from known quasar absorbers with measured H I column densities $\log[N(\mathrm{H\,I})/\mathrm{cm}^{-2}] > 18.0$ from Hubble Space Telescope (HST) UV spectroscopy. Early findings from the survey include the discovery of gas likely tied to the intragroup medium (IGrM; Péroux et al. 2017, 2019), accretion (Rahmani et al. 2018a), and galactic winds (Rahmani et al. 2018b). Both Klitsch et al. (2018) and Szakacs et al. (2021) combine MUSE data with ALMA data to investigate the molecular and ionized gas properties of galaxies at the same redshift as the H I absorbers. The molecular gas in associated galaxies extends further than the ionized disc (Klitsch et al. 2018) and is kinematically coupled with the ionized gas (Szakacs et al. 2021). Hamanowicz et al. (2020) investigated correlations between absorber and galaxy properties for a subsample of 14 absorbers. Our work is a continuation of that study for the full MUSE-ALMA Haloes survey. With this complete sample of 32 absorbers, we aim to examine the distribution of gas and metals in the CGM, and how this distribution is related to the properties of associated galaxies. We adopt the following cosmology: $\mathrm{H}_0 = 70$ kms^{-1} Mpc^{-1}, $\Omega_M = 0.3$, and $\Omega_\Lambda = 0.7$.

2 NEW MUSE OBSERVATIONS

The VLT/MUSE observations presented in this paper were carried out across various programmes (ESO 96.A-0303, 100-A-0753, 101.A-0660 and 102.A-0370, PI: C. Péroux and 298.A-0517, PI: A. Klitsch). For further details on the observing strategy, data reduction, and data quality checks (astrometry, wavelength, and flux calibration), we refer the reader to Péroux et al. (2022). For the sake of completeness, we summarize the detection methods here:

(i) Passive galaxies without detectable emission were found with a continuum search using the PROFOUND[1] tool (Robotham et al. 2018). The limiting continuum magnitudes are calculated within an aperture with radius equal to the seeing in a pseudo r-band image of the MUSE cube. Our calculated 3σ limits in Table 1 vary between MUSE fields because of the different exposure times and seeing conditions.

(ii) In addition to continuum sources, we expect a population of faint objects only detectable by their emission lines. To systematically search for these objects without continuum, we used the MUSE Line Emission Tracker (MUSELET) module of the MUSE Python Data Analysis Framework (MPDAF) package[2] (Bacon et al. 2016). For each absorber, we calculate the 3σ SFR limit. We assume the source is unresolved over a disc with diameter equal to the seeing and an emission line with full width at half-maximum (FWHM) of 3 Å. From this SFR limit, we estimate a stellar mass limit assuming the galaxy is on the main sequence (Schreiber et al. 2015). These values are tabulated in Table 1.

(iii) We also use complementary HST imaging from a 40-orbit medium programme (ID: 15939, PI: Peroux) and additional archival HST data. The fainter detection limit in the HST broad-band images enabled us to search for objects not detected by previous methods. This approach contributed 10 additional sources that were typically [O II] or Ly-α emitters missed by MUSELET. All continuum galaxies identified in the MUSE data were recovered in the HST data if the field was observed with a red HST filter (e.g. F702W and F814W).

(iv) Finally, we perform a spectral PSF subtraction of the QSO to search for objects at low separation in the MUSE cube using QFITSVIEW[3] (Ott 2012). This search was performed at the redshifts of H I absorbers to ensure no emission-line galaxies near the QSO were missed. The linemaps at the expected position of strong emission lines are created surrounding the background QSO, which effectively subtracts out the QSO continuum. A galaxy obscured by the QSO point spread function (PSF) in the field Q0454 + 039 was detected in this manner.

[1] https://github.com/asgr/ProFound
[2] https://mpdaf.readthedocs.io/en/latest/index.html#
[3] https://www.mpe.mpg.de/ ott/QFitsView/

Table 1. Summary of absorber properties targeted in the MUSE-ALMA Haloes Survey. Absorber redshifts, H I column densities and metal abundances are tabulated. We also include the survey area corresponding to the 60 × 60 arcsec^2 FoV of MUSE at the absorber redshift. For each field and absorber redshift, we provide 3σ SFR and equivalent stellar mass limits using the SFR-M_* main sequence. The number of galaxies within ±500 kms^{-1} of the quasar absorbers is also given in the penultimate column. The final column contains references for the absorber H I column density and metal abundance.

Quasar	z_{abs}	log N(H I) (cm^{-2})	(Zn/H) 12 + log (O/H)	(Fe/H) 12 + log (O/H)	Survey Area (kpc × kpc)	m_r limit mag	SFR limit (M$_\odot$ yr^{-1})	M_* limit (logM$_\odot$)	N_{gal}	Reference
Q0058 + 0019	0.6125	20.08 ± 0.15	0.08 ± 0.21	−0.01 ± 0.16	405 × 405	24.0	7.3×10^{-1}	9.1	0	P00, P00
Q0123 − 0058	0.8686	<18.62	–	–	463 × 463	23.2	3.1×10^{0}	9.6	0	R06
...	1.4094	20.08 ± 0.09	−0.45 ± 0.2	−0.25 ± 0.12	506 × 506	...	1.4×10^{1}	10	0	M09, M09
Q0138 − 0005	0.7821	19.81 ± 0.08	0.28 ± 0.16	>0.09	447 × 447	23.5	1.6×10^{1}	9.3	1	P08, P08
J0152 − 2001	0.3830	<18.78	–	>−1.36	314 × 314	25.6	2.8×10^{-2}	7.7	6	R18, H20
...	0.7802	18.87 ± 0.12	–	>−0.44	447 × 447	...	1.9×10^{-1}	8.4	1	R06, H20
Q0152 + 0023	0.4818	19.78 ± 0.08	–	–	359 × 359	24.6	2.4×10^{-1}	8.6	4	R06
Q0420 − 0127	0.6331	18.54 ± 0.09	–	–	411 × 411	25.2	1.1×10^{-1}	8.2	4	R06
Q0454 + 039	0.8596	20.69 ± 0.03	−1.01 ± 0.12	−0.73 ± 0.08	356 × 356	26.5	1.2×10^{-1}	8.3	2	P00, P00
...	1.1532	18.59 ± 0.02	–	–	360 × 360	...	2.7×10^{-1}	8.4	2	R06
Q0454 − 220	0.4744	19.45 ± 0.03	–	–	461 × 461	25.3	1.0×10^{-1}	8.3	1	R06
...	0.4833	18.65 ± 0.02	–	–	495 × 495	...	1.1×10^{-1}	8.3	1	R06
Q1110 + 0048	0.5604	20.20 ± 0.10	–	–	388 × 388	26.2	1.2×10^{-1}	8.3	3	R06
J1130 − 1449	0.1906	<19.10	–	–	191 × 191	25.7	4.0×10^{-3}	7.0	1	R06
...	0.3127	21.71 ± 0.08	–	−1.64 ± 0.08	275 × 275	...	1.8×10^{-2}	7.6	13	R06, P19
...	0.3283	<18.90	–	–	284 × 284	...	1.2×10^{-2}	7.4	2	R06
J1211 + 1030	0.3929	19.46 ± 0.08	–	>−1.05	319 × 319	25.3	3.5×10^{-2}	7.8	3	R06, H20
...	0.6296	20.30 ± 0.24	–	−0.68 ± 0.3	410 × 410	...	2.2×10^{-1}	8.5	2	R06, H20
...	0.8999	<18.50	–	–	467 × 467	...	3.9×10^{-1}	8.7	5	R06
...	1.0496	<18.90	–	>1.69	486 × 486	...	7.6×10^{-1}	8.9	0	R06, H20
Q1229 − 021	0.3950	20.75 ± 0.07	−0.5	<−1.31	320 × 320	24.9	4.4×10^{-2}	7.9	1	B98, B98
...	0.7572	18.36 ± 0.09	–	>−1.48	442 × 442	...	3.4×10^{-1}	8.7	1	R06, H20
...	0.7691	18.11 ± 0.15	–	>−2.34	444 × 444	...	3.4×10^{-1}	8.7	3	R06, H20
...	0.8311	18.84 ± 0.10	–	>−2.19	456 × 456	...	3.7×10^{-1}	8.7	4	R06, H20
Q1342 − 0035	0.5380	19.78 ± 0.13	–	–	380 × 380	24.1	4.4×10^{-1}	8.9	2	R06
Q1345 − 0023	0.6057	18.85 ± 0.20	–	–	403 × 403	25.4	1.9×10^{-1}	8.5	2	R06
Q1431 − 0050	0.6085	19.18 ± 0.24	–	–	404 × 404	25.1	2.6×10^{-1}	8.6	3	R06
...	0.6868	18.40 ± 0.07	–	–	425 × 425	...	3.7×10^{-1}	8.7	2	R06
Q1515 + 0410	0.5592	20.20 ± 0.19	<0.64	–	388 × 388	25.5	1.7×10^{-1}	8.4	4	R16, R16
Q1554 − 203	0.7869	<19.00	–	–	448 × 448	25.3	2.4×10^{-1}	8.5	1	R06
J2131 − 1207	0.4298	19.50 ± 0.15	–	>−0.96	337 × 337	25.6	7.1×10^{-2}	8.1	4	M16, H20
Q2353 − 0028	0.6044	21.54 ± 0.15	−0.92 ± 0.32	–	402 × 402	25.6	1.8×10^{-1}	8.5	0	R06, N08

B98: Boisse et al. (1998), H20: Hamanowicz et al. (2020), M09: Meiring et al. (2009), M16: Muzahid et al. (2016) N08: Nestor et al. (2008), P00: Pettini et al. (2000), P08: Péroux et al. (2008), P19: Péroux et al. (2019), R06: Rao, Turnshek & Nestor (2006), R16: Rahmani et al. (2016), and R18: Rahmani et al. (2018b).

Fig. 1 shows a white-light image of the Q1431 – 0050 field with all objects marked by how they were first detected. The dashed circles represent galaxies associated with the absorber at the redshift found in the legend. Similar white-light images of the remaining fields can be found in Appendix A.

Redshifts for all objects detected in the MUSE data were determined using the MARZ[4] tool (Hinton et al. 2016) and independently verified by two experts (SW and CP). We refer the reader to Péroux et al. (2022) for a more detailed methodology.

3 ASSOCIATED GALAXY PROPERTIES

3.1 Identification of galaxies associated with absorbers

The selection criteria for galaxies that are 'associated' with the H I Ly-α absorbers are critical to our study. We require galaxies to be within ±500 kms^{-1} of the absorber. This selection differs from previous survey papers (e.g. Hamanowicz et al. 2020, uses a ±1000 kms^{-1} window and includes three additional galaxies) because recent studies have shown that Mg II absorbers that trace dense, neutral gas are rarely detected beyond ±300 kms^{-1} (Huang et al. 2021). EAGLE simulations of more spatially extended ionized gas (O VI λλ1032, 1038) find that line-of-sight velocity cuts of ±500 kms^{-1} include significant amounts of gas beyond the virial radius (Ho, Martin & Schaye 2021). We expect the host galaxies of the dense and neutral absorbers in the MUSE-ALMA Haloes survey to be within a smaller velocity window than the O VI but maintain a velocity cut of ±500 kms^{-1} to be consistent with other surveys (Dutta et al. 2020). However, we note that other studies have used different criteria (e.g. Schroetter et al. 2016b; Berg et al. 2022). Absorber redshifts are tabulated in Table 1, and galaxy redshifts are obtained from the final catalogues of the MUSE-ALMA Haloes survey. The typical uncertainty in the galaxy redshift is 50–60 kms^{-1}. The velocity difference between the galaxy and the absorber is calculated using $\Delta v = c(z_{gal} - z_{abs})/(1 + z_{abs})$. We find 79 galaxies within ±500 kms^{-1} of 27 absorbers and we henceforth refer to this sample as associated galaxies. Included in this sample are six associated galaxy candidates that have low signal-to-noise ratio (SNR) emission or absorption features near the absorber redshifts. Five absorbers do not have galaxy counterparts. We note that 75 per cent of objects are found within ∼200 kms^{-1} of the absorber and 90 per cent within ∼350 kms^{-1}. If we restrict associated galaxies to be within ±300 kms^{-1} of absorbers, we still find that 27/32 absorbers have an accompanying galaxy.

In Table 1, we list the properties of the absorber and the number of associated galaxies (N_{gal}) found for each absorber. We flag the redshifts of the possible galaxy counterparts with quality 2 in Table 1 to be consistent with the catalogues in Péroux et al. (2022). For five

[4]https://samreay.github.io/Marz/#/overview

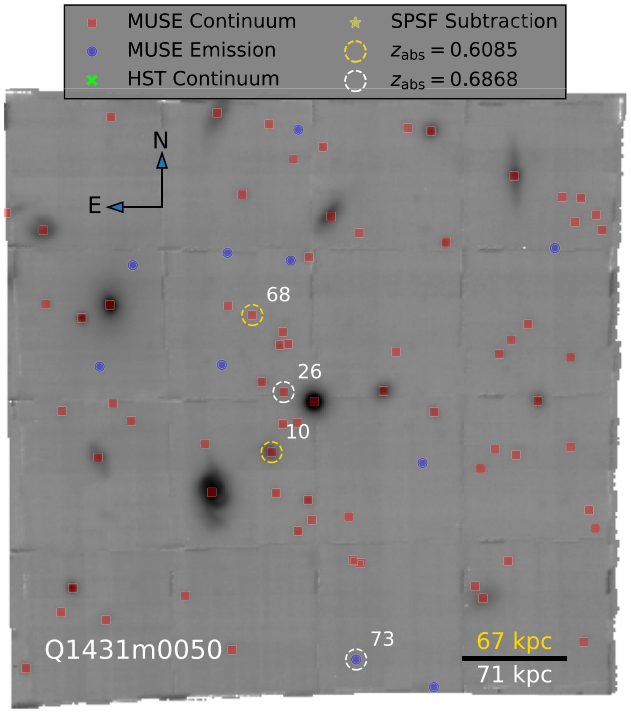

Figure 1. A white-light image of the MUSE field centred on quasar Q1431 – 0050. The four markers represent how the object was detected. Red squares denote continuum objects detected using PROFOUND and blue circles are emission-line sources. Green crosses are objects found after we used sources in the HST continuum imaging as a prior that were not found initially during our MUSE continuum and emission-line searches. Gold stars represent objects detected using a spectral PSF subtraction of the quasar. No objects are detected in the Q1431 – 0050 field using HST images as a prior and after a QSO subtraction, but we direct the reader to Figs A1, A2, and A3 for such instances. We note that many sources will be detected in multiple ways; an emission-line galaxy with bright stellar continuum will be found in MUSE continuum, emission, and in the HST continuum imaging. The markers only denote how the source was first detected, following the order of methods listed in Section 2 (using a MUSE continuum and emission-line search, HST continuum detections as a prior, and a spectral PSF subtraction of the QSO). The dashed circles are galaxies that are within ± 500 kms^{-1} of an absorber and they are labelled by their ID in the MUSE-ALMA Haloes object catalogues (Péroux et al. 2022). Ten arcseconds correspond to 67 and 71 kpc at $z_{abs} = 0.6085$ and $z_{abs} = 0.6868$, respectively. North is up and east is left.

absorbers in four fields, we do not detect any galaxies within ± 500 kms^{-1}.

3.2 Spectral extraction

The circular apertures used to extract spectra were checked to determine whether all the emission flux was captured. For sources with extended emission, the apertures were redrawn using the segmentation maps produced by PROFOUND or manually on QFITSVIEW using linemaps. This additional step was only necessary for three sources and ensures we have accurate measurements of the emission-line flux to determine properties such as SFR and metallicity.

3.3 Flux measurements

Initially, emission lines [O II] λλ3726, 3729, Hδ λ4102, Hγ λ4340, Hβ λ4861, [O III] λλ4959, 5007, [N II] λλ6549, 6583, Hα λ6563, and [S II] λλ6717, 6730 were automatically fitted using the MPDAF 1D Gaussian function. We inspected the quality of the fits and searched for cases where the continuum estimation (using a width of 40 pixels centred on the line) appeared incorrect. This was typically caused by emission lines being near the GALACSI Adaptive Optics (AO) gap centred on the rest-frame Na I D line or the presence of strong sky residuals. Lines near the AO gap required a custom and asymmetric window for continuum estimation while sky residuals were masked during the refit.

Broad stellar absorption around the Balmer lines was fitted out using the method from Zych et al. (2007), which involved simultaneously fitting the absorption and emission using two Gaussians. For the resolved [O II] doublet, a double Gaussian fit was used. Examples of these fits for associated galaxies in the Q1431 – 0050 field are shown in Fig. 2.

For galaxies at redshift $z \lesssim 0.42$, the observed Balmer decrement Hα/Hβ can be used to determine the dust attenuation. The intrinsic flux ratio of these lines is expected to be Hα/H$\beta = 2.87$ (Osterbrock 1989), assuming that case-B recombination and any deviation from this value is expected to be caused by dust. The colour excess $E(B-V)$ was calculated assuming a Small Magellanic Cloud-type (SMC-type) extinction curve (Pei 1992) using the prescription in Gharanfoli et al. (2007). It has been found that the average extinction curve in Mg II systems at redshift $1 \leq z_{abs} < 2$ resembles an SMC-type curve (York et al. 2006). Uncertainties were determined by propagating errors in the Hβ and Hα flux measurements.

4 RELATING ABSORBER AND GALAXY PROPERTIES

4.1 Distribution of galaxies

With the associated galaxy sample finalized, we can begin investigating the relationships between CGM gas properties such as H I column density and the properties of the associated galaxies. Early studies connecting H I absorbers with nearby galaxies typically found a single associated object (e.g. Bergeron 1986b; Bergeron & Boissé 1991). Later works that build significant samples of absorber-galaxy systems use longslit or multislit spectroscopy on objects seen in imaging of the QSO field (e.g. Chen & Mulchaey 2009; Ribaudo et al. 2011; Thom et al. 2011; Lehner et al. 2013). These methods bias against detections of galaxies at very small angular separations to the QSO. In 7 out of the 19 fields (e.g. Q0454 + 039 at $z_{abs} = 0.8596$ and Q1110 + 0048 at $z_{abs} = 0.5604$), we find galaxies within 3 arcsec of the QSO. Many of these earlier works that rely on imaging and then spectroscopy are incomplete in this regard. Moreover, galaxies with faint continuum will also be missed in imaging; the ability of IFS to simultaneously search for continuum and emission objects has greatly improved the completeness of searches for absorber–galaxy pairs and recent surveys often find that multiple galaxies can be associated with a single absorber (Hamanowicz et al. 2020; Chen et al. 2020a; Berg et al. 2022).

We also note there are various targeted surveys of the CGM surrounding isolated galaxies (e.g. Tumlinson et al. 2013; Liang & Chen 2014; Borthakur et al. 2015; Prochaska et al. 2017; Berg et al. 2018; Chen et al. 2018; Pointon et al. 2019; Kulkarni et al. 2022). These 'galaxy-centric' surveys cross-correlate background quasar sightlines with foreground galaxies pre-selected by their properties. In this work, we choose to plot results from 'absorber-centric' surveys, where the pre-selection is based on the absorber properties and the types of galaxies and environments studied vary more significantly.

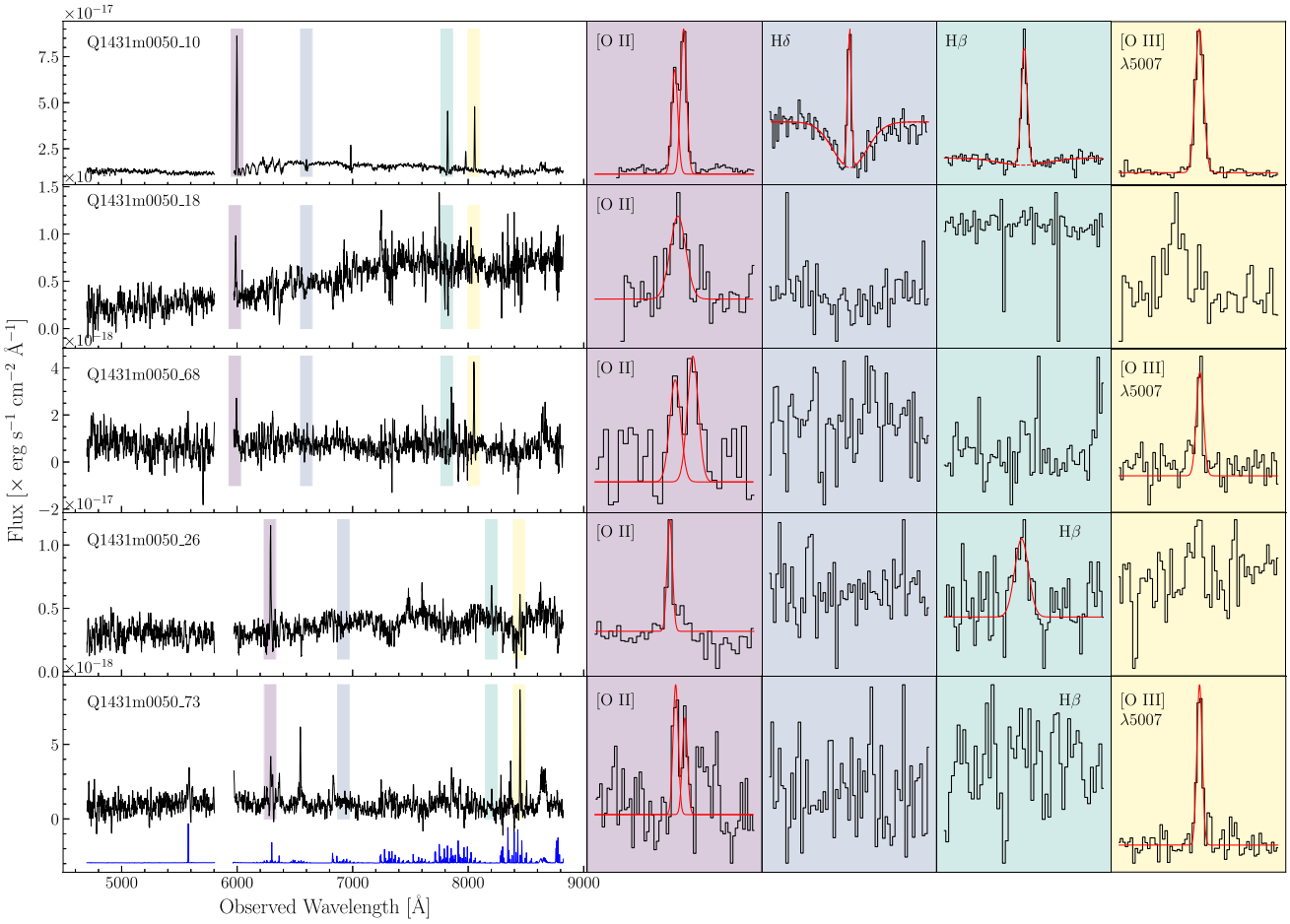

Figure 2. The spectra of galaxies associated with absorbers in the Q1431 – 0050 field and corresponding emission-line fits. The left-hand panels show the MUSE spectra of the associated galaxies after smoothing with a 5-pixel boxcar, and the galaxy identification from the MUSE-ALMA Haloes catalogues is displayed in the top left. In the bottom-left panel, a sky spectrum is included in blue. The right-hand panels show our [O II], Hδ, Hβ, and [O III] λ5007 emission-line fits in red to unsmoothed spectra. The background colours correspond to the boxed emission lines in the full spectra. We present a variety of different emission-line fits here: a double Gaussian for [O II] (e.g. objects Q1431m0050_10 and Q1431m0050_68) and emission with stellar absorption (two centre panels for object Q1431m0050_10). We also display non-detections of emission lines in the spectra.

In Fig. 3, we plot the distribution of associated galaxies around absorbers in physical space. We only include galaxies found within a 191 kpc × 191 kpc region centred on the QSO. This corresponds to the MUSE areal coverage of the $z = 0.1906$ absorber and reduces the sample of associated galaxies to 41. The overlaid 2D kernel density estimation reveals the probability of finding an associated galaxy is higher at close separations to the absorber. The surface density map is not centred on the absorber (red cross), but this is likely caused by the variability in small samples.

Fig. 4 reveals that 17 out of the 32 (59 per cent) absorbers have two or more objects within ±500 kms^{-1} of the neutral gas. We also find that the distribution of column densities varies significantly for each bin of the number of associated galaxies. While we expect high H I column density systems to be associated with galaxies at smaller impact parameters (Péroux et al. 2005; Noterdaeme et al. 2014), it remains unclear whether the environment of absorbers depends on N(H I). Recent works using multiple QSO sightlines or an extended background source reveal >1 dex changes in column density across separations of only several kpc (Augustin et al. 2018; Kulkarni et al. 2019; Cashman, Kulkarni & Lopez 2021; Bordoloi et al. 2022), suggesting N(H I) likely does not correlate with the number of associated galaxies because gas in the CGM is inhomogeneously distributed.

To test this, in Fig. 5, we plot the number of associated galaxies normalized by the physical area of the MUSE FoV found for a given absorber column density. We expand the MUSE-ALMA Haloes sample to lower column densities using the CUBS (Chen et al. 2020a) and BASIC (Berg et al. 2022) surveys and only include absorbers observed with MUSE. The median $N_{\rm gal}$ value using 1 dex bins in the range $16.0 < \log[N(\mathrm{H\,I})/\mathrm{cm}^{-2}] < 22.0$ is plotted in red. There appears to be no correlation between the column density of the H I and the number of associated galaxies detected after controlling for the different physical scales probed by MUSE at the various absorber redshifts. While we find a rich galaxy group associated with our highest column density system ($\log[N(\mathrm{H\,I})/\mathrm{cm}^{-2}] = 21.71 \pm 0.08$ for $z_{\rm abs} = 0.3127$ in J1130-1449), there is no galaxy near the Q2353-0028 absorber with $\log[N(\mathrm{H\,I})/\mathrm{cm}^{-2}]$=21.54 ± 0.15 and $z_{\rm abs}$ = 0.6044 down to a SDSS r-band magnitude of ∼25 and SFR limit of 0.18 M$_\odot$ yr^{-1}. The large median value in the final bin is caused by the significant overdensity in the former system, and we require more observations of $\log[N(\mathrm{H\,I})/\mathrm{cm}^{-2}]$>21.0 absorbers for a statistically significant result.

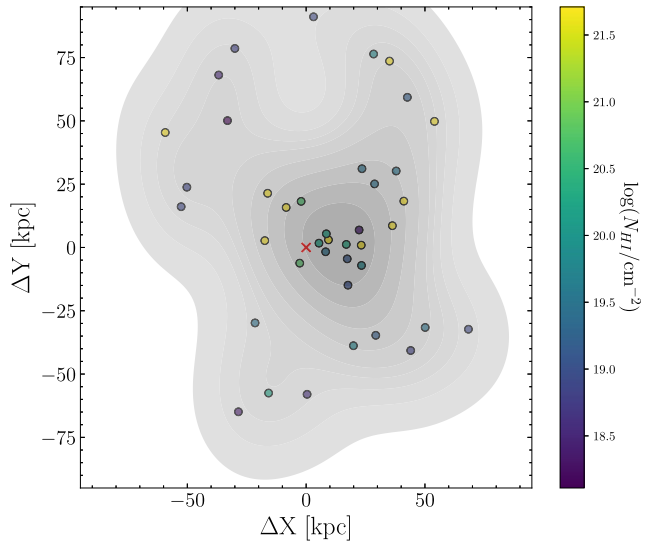

Figure 3. The distribution of associated galaxies around absorbers using their physical distances from the absorber (red cross). Each galaxy is coloured by the H I column density of the absorber they are associated with. We use a 2D Gaussian kernel density estimator to construct a surface density map of the associated galaxies. The darker areas represent regions of high density. We limit the associated galaxies plotted to those within the area covered by the MUSE FoV of the lowest redshift absorber ($z_{\rm abs} = 0.1906$ corresponding to 191 kpc × 191 kpc). There are 41 galaxies within this area.

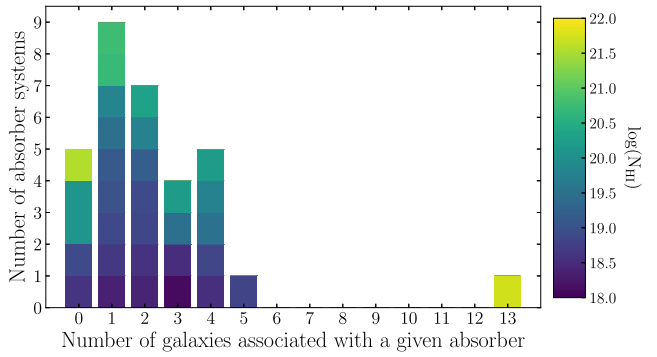

Figure 4. The number of associated galaxies ($N_{\rm gal}$) identified per absorber. Each absorber is colour-coded by its H I column density. 17 out of the 32 absorbers (53 per cent) with MUSE IFS observations have at least two associated galaxies. It appears that there is no trend between $N_{\rm H\,I}$ and the number of associated galaxies.

While the majority of the absorbers in the MUSE-ALMA Haloes survey are associated with more than one galaxy, connecting the absorber to a 'most probable host galaxy' is useful when studying the distribution of gas in the CGM. Traditionally, the galaxy closest in impact parameter to the absorber has been designated as the most probable host (Schroetter et al. 2016b), and we also choose to adopt this method. The distribution in impact parameter, b, and velocity space, Δv, of the associated galaxies is depicted in Fig. 6. The diamonds represent galaxies that are closest in impact parameter to the absorber and for two-thirds of the absorbers with associated galaxies (18/27); these galaxies also have the smallest velocity separation to the absorber. We also find that the distribution in b is not uniform, with the majority of galaxies found <100 kpc from the absorber. This effect is partly caused by the wide range of absorber redshifts ($0.20 \lesssim z \lesssim 1.4$) corresponding to physical scales of 100–

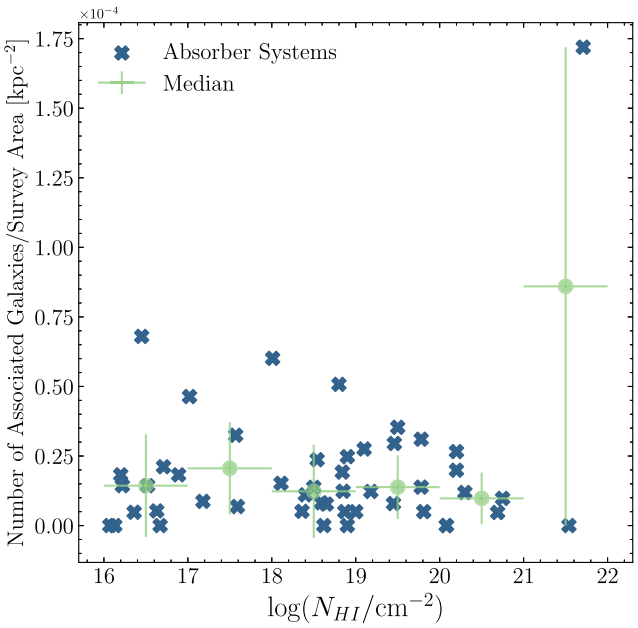

Figure 5. The number of galaxies associated with a given absorber ($N_{\rm gal}$) normalized by the survey area plotted against the absorber column density. We include in this plot absorbers analysed with MUSE data from the CUBS and BASIC surveys. The green points give the median value in 1 dex bins of H I column density from $\log[N({\rm H\,I})/{\rm cm}^{-2}] = 16.0 - 22.0$. The error in the median value of $N_{\rm gal}$/area is calculated using the standard deviation of values within a given bin. We find that this value does not evolve with the column density of the absorber. The large median value in the highest column-density bin is attributed to a 13-member galaxy group associated with a single absorber at $z_{\rm abs} = 0.313$.

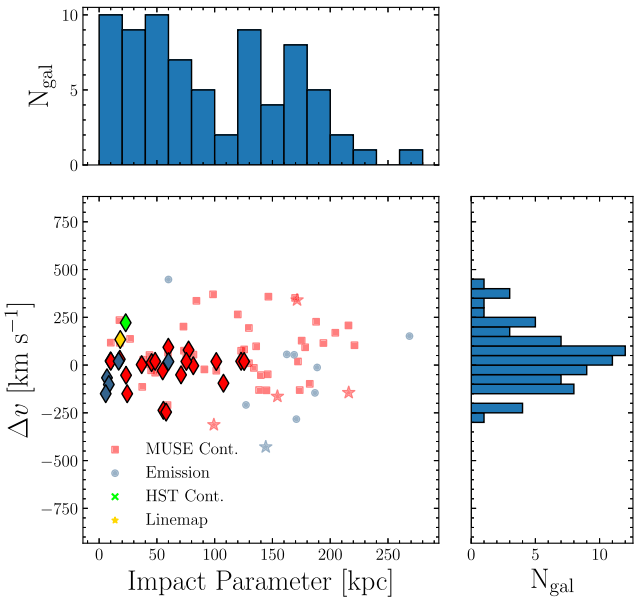

Figure 6. The distribution of associated galaxies in impact parameter and velocity space. The galaxy velocities appear to peak near the absorber redshift, with an extended tail at large positive velocities. More galaxies are found at low impact parameters, but this effect may be caused by the MUSE FoV, limiting the areal coverage at low redshifts. Galaxies are labelled by how they were detected using the colour scheme in Fig. 1. Stars represent the sample of six possible associated galaxies. For this and the following figures, diamonds represent galaxies that are closest in impact parameter to the absorber (most probable host galaxies).

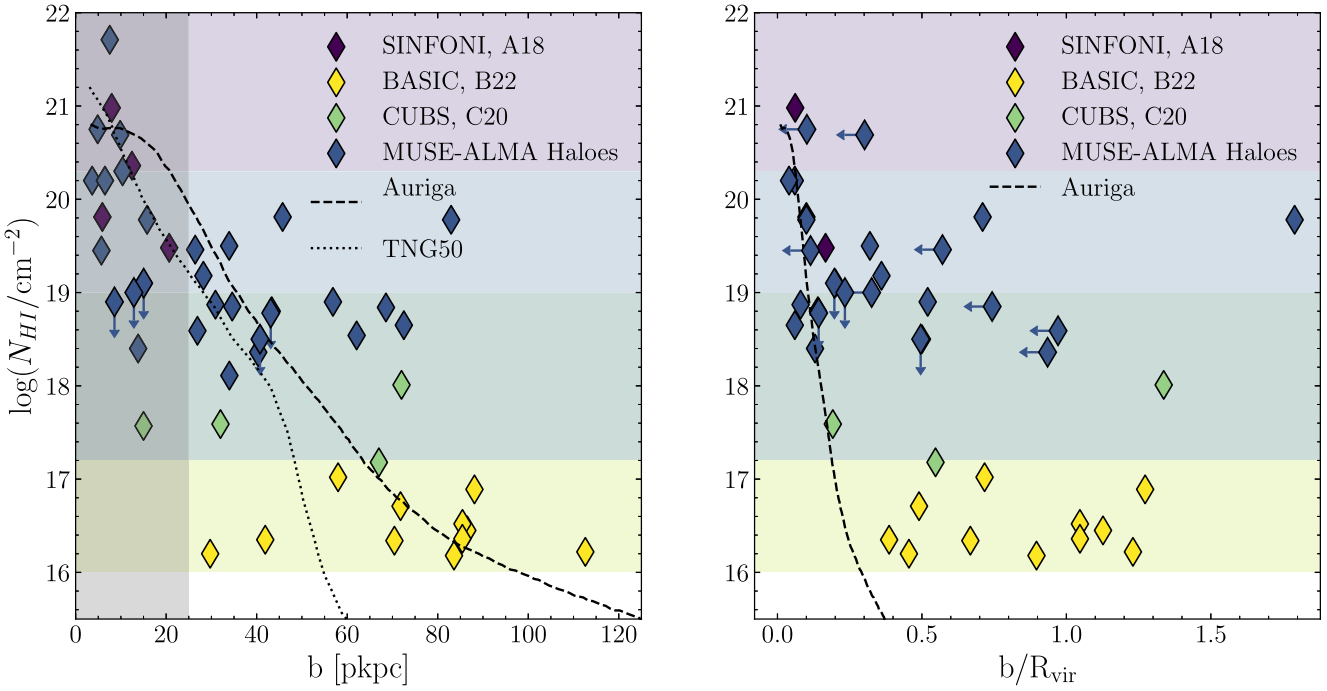

Figure 7. The H I column density of absorbers against the impact parameters of associated galaxies. The galaxies closest in impact parameter to the absorber are plotted here as diamonds. We include data from SINFONI surveys of galaxy counterparts to absorbers (A18; Augustin et al. 2018), the BASIC (B22; Berg et al. 2022), and the CUBS (C20; Chen et al. 2020a) to extend our results to higher and lower column densities. The coloured regions from top to bottom represent DLA, sub-DLA, LLS, and pseudo-LLS column densities, while the grey region marks the inner 25 kpc where ISM gas is likely responsible for the absorption. The median radial profiles for the neutral hydrogen column density from the simulations by van de Voort et al. (2019) and Nelson et al. (2020) are respectively plotted as dashed and dotted lines. In the right plot, we normalize the impact parameter by the virial radius. For galaxies without stellar mass measurements, we derive an upper limit for the stellar mass using the SFR limit for each field and assuming the galaxy lies on the SFR-M_* main sequence (Schreiber et al. 2015). Passive galaxies will shift the limits leftward towards smaller values of $b/R_{\rm vir}$ (see Appendix C for the calculation). Both plots reveal a scatter of ∼3 dex in $N_{\rm H\,I}$ at a given impact parameter, but also a clear decrease in log N(H I) at higher b.

250 kpc for an angular separation of 30 arcsec. The distribution of velocity differences between absorber and galaxy is found to be symmetric about $\Delta v = 0$ kms^{-1} with a tail at large positive Δv. To test whether the tail is statistically significant, we split the sample into two using the sign of Δv. Then, we take the absolute value of the sample with $\Delta v < 0$ and perform a two-sided Kolmogorov–Smirnov test to determine whether the two partitions are drawn from the same population. We find a p-value of approximately 0.3, suggesting that the Δv values of our associated galaxies are symmetrically distributed about 0.

In the left-hand panel of Fig. 7, we plot log N(H I) against b for galaxies closest in impact parameter (min (b)) to the absorber. We apply this criteria to the BASIC (Berg et al. 2022) and CUBS (Chen et al. 2020a) surveys and extend our results to lower column densities. Additionally, we include detections from early IFS studies that use the Spectrograph for INtegral Field Observations in the Near Infrared (SINFONI) instrument to search for galaxy counterparts to high column-density absorbers (e.g. Bouché et al. 2007, 2013; Schroetter et al. 2015; Péroux et al. 2016). Our $N_{\rm H\,I}(b)$ results when combined with previous surveys enable a comparison with simulations of the CGM. van de Voort et al. (2019) uses zoom-in magnetohydrodynamic simulations of a Milky Way-mass galaxy from the Auriga project (Grand et al. 2017) and performs an additional uniform spatial refinement to enhance the physical scales resolved in the CGM. In Fig. 7, we plot the median radial profile of the neutral hydrogen column density for the highest resolution simulation (≈1 kpc spatial resolution of the CGM) using a dashed line. Similarly, Nelson et al. (2020) study the distribution of cold gas in the CGM around massive galaxy group haloes (∼$10^{13.5}$ M$_\odot$) at $z \sim 0.5$ by post-processing TNG50, the lowest volume and highest resolution simulation from the Illustris-TNG suite. Within a third of the virial radius, sub-kiloparsec resolutions are reached and this increases to ≈3 pkpc at $R_{\rm vir}$. We choose to include both these simulations because the systems probed by H I absorbers have been found to be associated with isolated galaxies and galaxy groups. While there appears to be agreement between the IFS observations and the median radial profile obtained from these hydrodynamical simulations out to ∼120 pkpc, we note that the H I versus b relation depends on the galaxy stellar mass. The median stellar mass log $M_* = 9.8$ of the MUSE-ALMA Haloes sample is lower than a Milky Way-mass galaxy.

We emphasize that different criteria can be used to select the most probable host galaxy of the H I gas. In Appendix B, we reproduce Fig. 7 by forcing the associated galaxy to be closest in both impact parameter (min (b)) and velocity (min ($|\Delta v|$)) to the absorber. This reduces the size of the MUSE-ALMA Haloes sample (18/27 associated galaxies remain), but increases the probability that the absorber is tied to the most probable host. The application of these criteria reduce the scatter in log N(H I) at a given impact parameter. However, the fact that numerous galaxies are found associated with these absorbers suggests gas in the CGM is not connected to the single halo of an isolated galaxy. In the zoom-in simulation of the CGM for a Milky Way-mass galaxy, the 1σ scatter in column density is >3 dex at $b = 50$ kpc (van de Voort et al. 2019). For larger halo masses ($10^{13.2}$ − $10^{13.8}$ M$_\odot$) at $z \sim 0.5$, Nelson et al. (2020) finds column densities

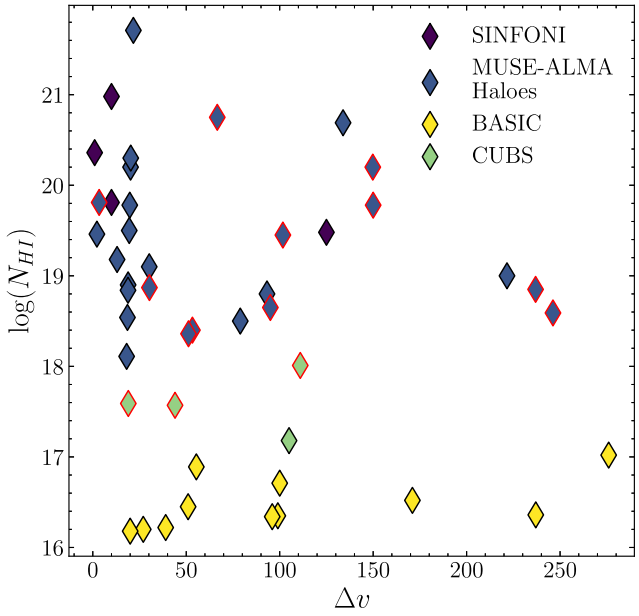

Figure 8. The H I column density of absorbers against the velocity difference of associated galaxies. Only the most probable hosts are plotted. Diamonds with a red border indicate the galaxy is found at negative velocities compared to the absorber redshift. For objects from the BASIC survey, the tabulated velocity differences in Berg et al. (2022) did not have a sign. We find that the galaxies associated with high column density absorbers are not necessarily close (within 50 kms^{-1}) to the absorber redshift.

ranging from $\log[N(\mathrm{H\,I})/\mathrm{cm}^{-2}]$=14 to 20 at an impact parameter of 50 pkpc within a 1σ scatter band. The significant observed scatter in the H I column density at any given b appears to be an intrinsic property of the CGM that is also found in simulations and this will be discussed further in Section 5.3.

As the stellar masses of associated galaxies vary significantly in the sample, a more physical representation of the impact parameter can be obtained by normalizing it with respect to the virial radius and this is shown in the right-hand panel of Fig. 7. We note that the stellar masses are derived using spectral energy distribution (SED) fitting of the HST and MUSE data, and this will be published in another work (Augustin et al., in preparation). We include also upper limits for galaxies where no SED fitting to determine the stellar mass could be performed. The upper limits are derived from the SFR limit for each field assuming the galaxy is on the SFR-M_* main sequence (Schreiber et al. 2015). While we find the majority of associated galaxies lie on the main sequence (Augustin et al., in preparation), passive galaxies will shift the limits leftward towards smaller values of $b/R_{\rm vir}$. This is because our estimates of galaxy virial mass use a stellar-to-halo mass relation (Navarro et al. 1997; Shull 2014; Rodríguez-Puebla et al. 2017) and passive galaxies will have a larger stellar mass for a given SFR (see Appendix C for the calculation). The results reveal a drop in $\log N(\mathrm{H\,I})$at $b/R_{\rm vir} > 0.5$, but also variations up to ∼3 dex in H I column density at a given impact parameter. When compared with a simulated Milky Way-mass galaxy with virial radius 337 kpc (van de Voort et al. 2019), the decline in H I column density is not as precipitous.

We find little correlation between the absorber H I column density and the velocity difference between $z_{\rm abs}$ and the galaxy at the lowest impact parameter in Fig. 8. At $|\Delta v| < 50$ kms^{-1}, the column density spans more than five orders of magnitude. This is unsurprising because the variety in the origin of absorbers means that the velocity difference should not relate to the column density. Previous works from the MUSE-ALMA Haloes survey already find the absorber attributed to large rotating discs with $V_{\rm max} = 200$ kms^{-1} ($\Delta v \sim 50$ kms^{-1}; Péroux et al. 2017), cold-flow accretion ($\Delta v \sim 80$ kms^{-1}; Rahmani et al. 2018a), and outflowing gas ($\Delta v \sim 110$ kms^{-1}; Rahmani et al. 2018b).

4.2 Galaxy star formation rates

We calculate the SFRs of associated galaxies using the H α emission line when available. For sources at redshift $z \gtrsim 0.4$ where H α is not observable with MUSE, we estimate the SFR using the [O II] luminosity. There is a median discrepancy of ∼40 per cent in the SFRs calculated using H α and [O II] emission-line fluxes for the 20 associated galaxies with both lines detected. The prescriptions from Kennicutt (1998) are used to determine the SFR to keep our results consistent with past MUSE-ALMA Haloes papers (Hamanowicz et al. 2020). For galaxies with dust corrections available, we also provide a dust-corrected SFR. 3σ SFR limits are calculated for non-detections assuming the FWHM of the line profile is 3 Å and the emission is found in the number of pixels contained within a disc with diameter equal to the seeing. For each galaxy, we categorize them as star forming (SF) if emission lines are present in the spectrum or passive if they are not. More rigorous criteria based on our SFR calculations are difficult to apply because the majority of the associated galaxies do not have extinction measurements. These values are tabulated in Table 2.

From Fig. 9, we find the SFRs of associated galaxies span >2 dex. We find that the most probable galaxy hosts typically have larger SFRs than other members in their group. This trend is clearer in the right-hand panel of Fig. 9, where the most probable host galaxies at larger impact parameters appear to have higher SFRs. However, the lack of dust corrections for ∼70 per cent of our sample inhibits any interpretation of these results.

4.3 Galaxy emission-line metallicity

The extensive redshift range of the absorbers ($0.2 \lesssim z \lesssim 1.40$) means different emission lines are seen for galaxies at different redshifts. Additionally, only galaxies at redshift $z < 0.4$ can be corrected for dust using the H α/H β Balmer decrement. We choose to use the $R_3 = \log(F([\mathrm{O\,III}]\lambda5007)/F(\mathrm{H}\beta))$ auroral strong-line calibration from Curti et al. (2017, 2020a) to calculate galaxy metallicities. This has the advantage of covering the required emission lines [O III] and Hβ up to $z \sim 0.85$ and being largely unaffected by dust obscuration. For objects below redshift 0.4, we also measure $\mathrm{O_3N_2} = \log(F([\mathrm{O\,III}]\lambda5007)/F(\mathrm{H}\beta))/\log(F([\mathrm{N\,II}]\lambda6584)/F(\mathrm{H}\alpha))$ (Pettini & Pagel 2004) to obtain a check of our $\mathrm{R_3}$ measurements and, in some cases, break the degeneracy in the double-branched $\mathrm{R_3}$ indicator. Upper and lower limits are given for objects without detectable flux in the [O III] and Hβ emission lines.

Metallicity errors are calculated by first determining $\Delta\mathrm{R_3}$ and $\Delta\mathrm{O_3N_2}$ by propagating the flux measurement errors. We then use Monte Carlo sampling to determine the errors in the roots of the polynomial that we solve to calculate the emission metallicity. We report our final metallicity values in Table 2. For consistency, only metallicities calculated using the $\mathrm{R_3}$ calibration are reported, but we note that for galaxies with both $\mathrm{R_3}$ and $\mathrm{O_3N_2}$ measurements, the metallicity values agree within their 1σ errors.

We find no significant trend between galaxy metallicity and absorber column density in the left-hand panel of Fig. 10. However, we find that the galaxy metallicities are typically subsolar (assuming

Table 2. Summary of associated galaxy properties. The identifications of galaxies within ±500 kms^{-1} of an absorber. Velocity differences (Δv) are calculated with respect to the absorber redshift. SFRs and limits are based on Kennicutt (1998), and we use the Hα empirical relation when available. At $z \gtrsim 0.4$, we use the [O II] λλ3726, 3729 luminosity to estimate the SFR. Dust corrections are performed for galaxies with measured Hβ and Hα emission-line fluxes. The tabulated values assume a Salpeter initial mass function (IMF; Salpeter 1955) and choosing to adopt the Chabrier IMF (Chabrier 2003) will reduce the SFRs by a factor of 1.8. Both R_3 lower and upper branch metallicites derived from Curti et al. (2017, 2020a) are provided when available. The extinction calculated using the Balmer decrement and galaxy type (SF or passive) are also provided. Galaxies are classed as SF if emission lines are seen in the spectrum and passive (P) if not. The redshift confidence (RC) is also given where a value of 2 indicates a possible associated galaxy due to low SNR absorption or emission lines. A value of 3 is a likely redshift where multiple high SNR lines are detected. Entries with value −999 correspond to measurements that are unavailable. For example, corrected SFRs are unavailable for galaxies without detectable or measurable Hβ and Hα emission. A complete table of associated galaxies and their properties is available online.

ID	z_{gal}	b (kpc)	Δv (kms^{-1})	SFR ($M_\odot$ yr^{-1})	SFR$_{corr}$ ($M_\odot$ yr^{-1})	$12+\log(O/H)_{lower}$	$12+\log(O/H)_{upper}$	$E(B-V)$	Type	RC
Q0138 − 0005, $z_{quasar} = 1.96$, $z_{abs} = 0.7821$, $\log[N(H\,I)/cm^{-2}] = 20.08 \pm 0.15$										
Q0138m0005_14	0.7821	82	−3.4	6.9 ± 2.4	−999	−999	8.7 ± 0.1	−999	SF	3
Q0152 − 2001, $z_{quasar} = 2.06$, $z_{abs} = 0.3830$, $\log[N(H\,I)/cm^{-2}] < 18.78$										
Q0152m2001_4	0.3814	180	340	<0.06	−999	−999	8.6 ± 0.2	−999	P	3
Q0152m2001_5	0.3826	60	84	0.73 ± 0.4	2.2 ± 0.5	−999	8.6 ± 0.1	0.53 ± 0.04	SF	3
Q0152m2001_7	0.3814	150	350	0.18 ± 0.4	−999	−999	<8.7	−999	SF	3
Q0152m2001_13	0.3815	84	330	0.10 ± 0.4	0.1 ± 0.4	−999	8.7 ± 0.1	0.019 ± 0.002	SF	3
...	...	...	...	...	...	...	...	...	...	...

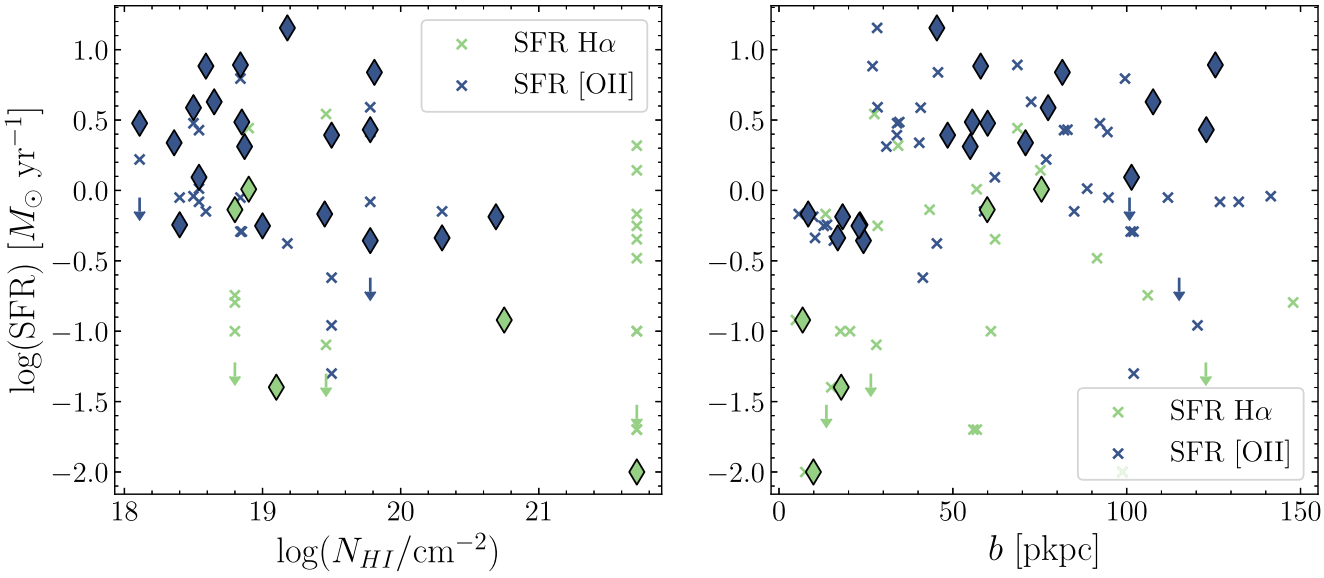

Figure 9. The SFRs of associated galaxies plotted against H I column density (left) and impact parameter (right). The SFR values use the Hα and [O II] luminosity calibrations from Kennicutt (1998). Associated galaxies closest in impact parameter to the QSO sightline are plotted as diamonds.

$(12+\log(O/H)) = 8.69$; Asplund et al. 2009). The right-hand panel of the same figure plots galaxy metallicity against impact parameter and again appears largely scattered.

Roughly half the absorbers in the sample (17/32) have Zn or Fe abundance measurements or limits from the literature. We preferentially adopt the [Zn/H] metallicity when available because Zn is typically not significantly depleted onto dust in the ISM (Spitzer & Jenkins 1975; Savage & Sembach 1996; Jenkins 2009; Vladilo et al. 2011). Otherwise, we correct our [Fe/H] measurements for dust by adding 0.3 to the original [Fe/H] value (Rafelski et al. 2012). Seven absorbers with metallicity limits have $\log[N(H\,I)/cm^{-2}] < 19.5$ where an ionization correction might be applicable.

We plot the galaxy emission metallicities found using the R_3 calibration against the absorber metallicity. Fig. 11 reveals that the emission-line metallicities are higher than the metallicities probed by absorbers in the CGM of galaxies. This finding broadly agrees with previous comparisons between galaxy and CGM metallicities where a gradient is found, but the scatter is large (Chen, Kennicutt & Rauch 2005; Christensen et al. 2014; Péroux, Kulkarni & York 2014).

The comparison between galaxy and absorber metallicity requires careful interpretation. Emission-line diagnostics, such as R_3 and O_3N_2, measure the integrated oxygen abundance in a galaxy. On the other hand, the absorption metallicity is a measure of the Zn or Fe abundance in a pencil-beam sightline intersecting gas in the CGM at some impact parameter from the galaxy centre. The correlation between this emission metallicity and the Zn or Fe abundance found in gas clouds is unclear. However, we find that the majority of galaxies have H II region metallicities in their inner regions that are much higher than those measured in absorption in their outskirts. These differences are significantly larger than those expected from an intrinsic enhancement in the ratio [O/Fe] compared to solar. Thus, the offsets we see in Fig. 12, where we show the metallicity

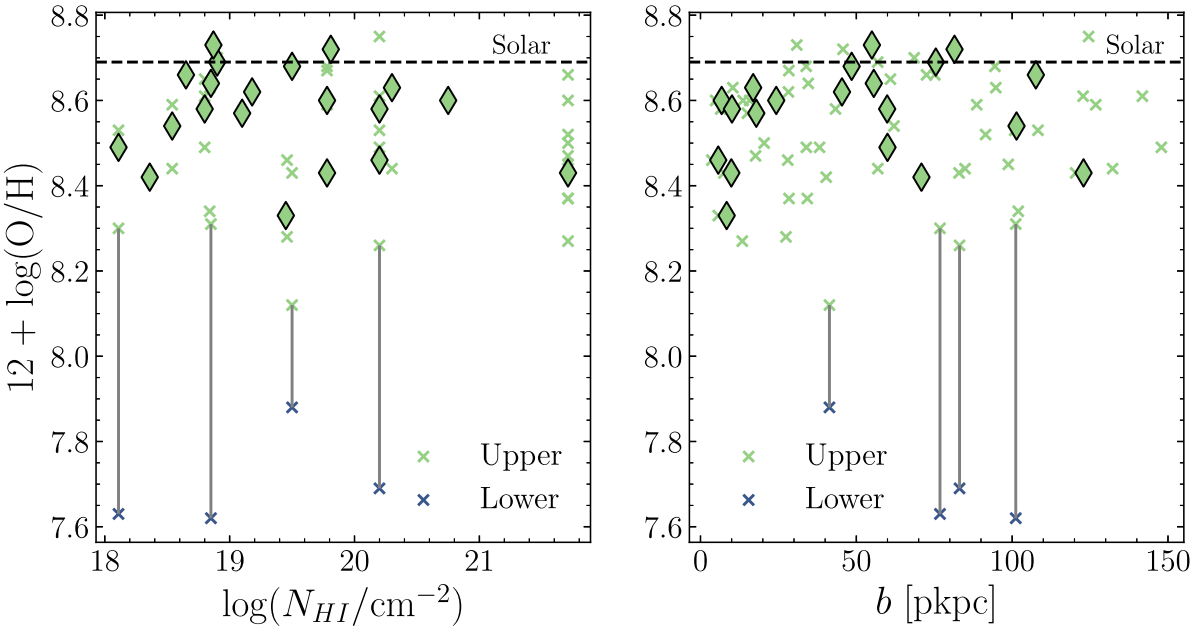

Figure 10. We plot the upper and lower branches of the associated galaxy sample using the R_3 metallicity calibration. If no O_3N_2 measurement is available to break the degeneracy, a grey line is used to connect the upper- and lower-branch measurements. The dashed line indicates the solar metallicity $(12 + \log(O/H)) = 8.69$ from Asplund et al. (2009). Like in previous plots, the most probable host galaxies are denoted by diamonds. The left-hand and right-hand panels reveal no trend between the metallicity of the associated galaxy and H I column density or impact parameter, respectively.

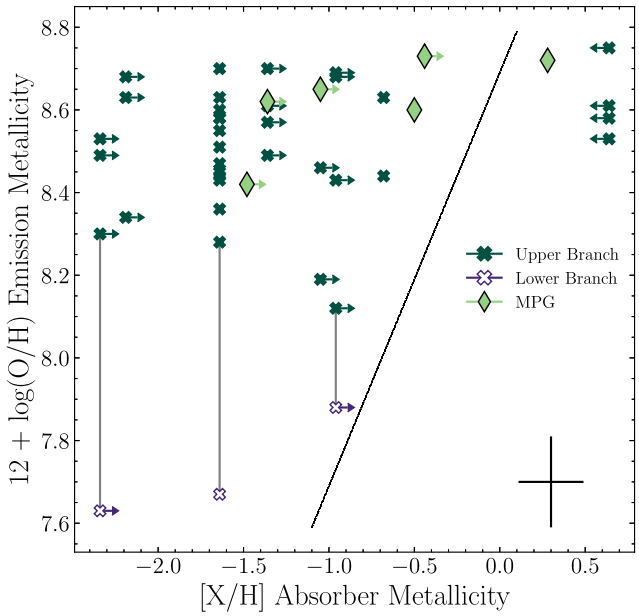

Figure 11. The absorber metallicity compared with the galaxy emission-line metallicity. The most probable galaxy hosts of the H I absorbers are denoted by the diamonds, while the remaining galaxies are crosses. Vertical lines connect the upper and lower branch galaxy metallicities that are degenerate using the R_3 calibration. 17 out of the 32 absorbers have metallicity measurements [Zn/H] or [Fe/H] and 10 of these measurements are limits. The dotted line denotes the line of equal galaxy and absorber metallicity. We find that the metallicity measured from strong-line diagnostics is typically larger than the CGM absorbing gas.

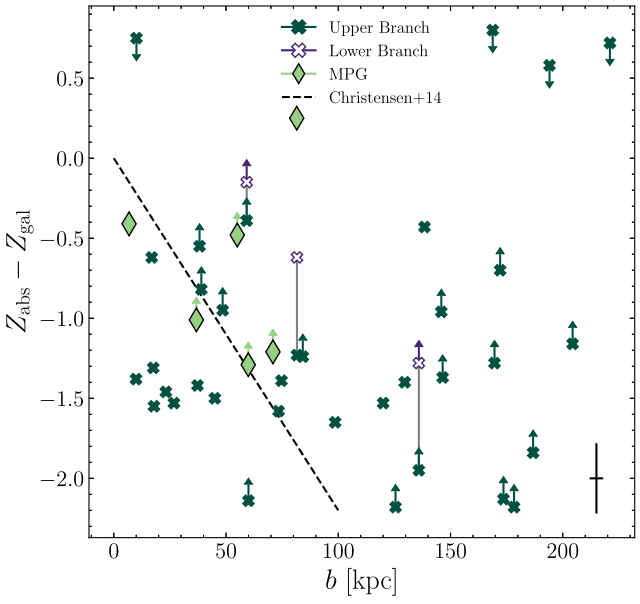

Figure 12. The difference in absorber and galaxy metallicity plotted against impact parameter. The most probable galaxy hosts of the H I are denoted by the diamonds, while the remaining galaxies are crosses. We include results from previous works studying damped Lyman-α absorbers and their host galaxies (Péroux et al. 2013; Christensen et al. 2014). Vertical lines connect the upper and lower branches galaxy metallicities that are degenerate using the R_3 calibration. The measured dependence of metallicity on impact parameter from Christensen et al. (2014) is included as a dashed black line.

difference between the absorber and the galaxy as a function of impact parameter, are caused by more than just a mismatch in the elements used to deduce the metallicity.

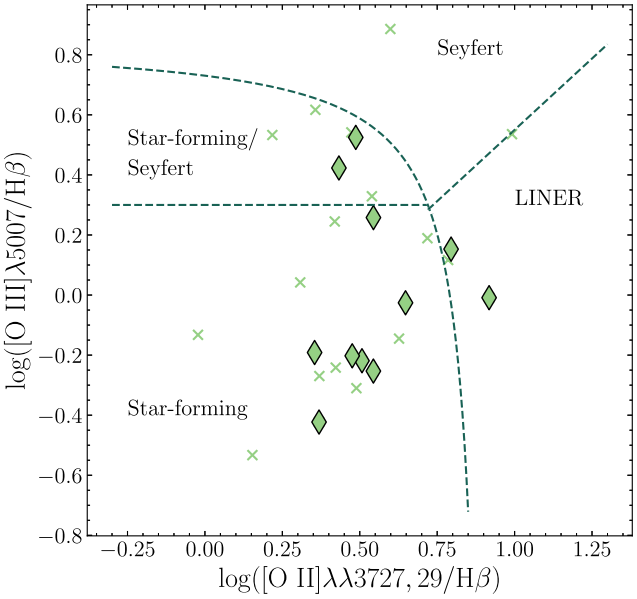

Figure 13. The [O III]/H β versus [O II]/H β classification diagram for galaxies associated with H I absorbers. The dashed line represents the empirical separation between SF galaxies, Seyfert 2 galaxies and LINERs.

For the galaxy associated with the absorber towards Q0138 − 0005 at $z_{\rm abs} = 0.7821$, we find the absorption metallicity to be larger than the emission-line metallicity of the galaxy (top-right diamond in Fig. 11). This is unusual because we expect the absorber abundance measurement to be significantly lower than the mean metallicity of the galaxy at an impact parameter of 81 kpc (Christensen et al. 2014). However, for this field, we reach a limiting magnitude limit of only $m_r = 23.5$, and it is possible that the QSO sightline intersects a fainter, undetected galaxy at smaller impact parameters. Further discussion on the non-detections of galaxy counterparts to the five absorbers can be found in Section 5.1.

4.4 [O III]/H β versus [O II]/H β diagram

For absorbers with $z_{\rm abs} \gtrsim 0.4$, the absence of H α and [N II] means the classical Baldwin, Phillips & Terlevich (BPT) diagram (BPT 1981) cannot be used to distinguish between SF galaxies and AGNs. Instead, we use the blue classification diagram from Lamareille (2010) to separate our sample into SF, Seyfert 2, and low-ionization nuclear emission-line region (LINER) galaxies. Equivalent width (EW) ratios of [O III] λ5007/H β and [O II]$\lambda\lambda$3727, 29/H β are computed for all associated galaxies. We exclude galaxies with continuum levels below 5×10^{-19} erg s^{-1} cm^{-2} Å adjacent to the relevant lines to ensure our EW measurements are accurate. Additionally, we limit the sample to galaxies with SNR >3 in [O II], H β, and [O III] emission. The wavelength range of MUSE also limits the redshifts of galaxies in this sample to $0.26 \lesssim z \lesssim 0.85$.

In Fig. 13, we plot the 27 associated galaxies that meet the aforementioned criteria on the classification diagram. We find that 16/27 galaxies are SF, with the remainder being placed in the Seyfert 2 and LINER regions of the diagram.

5 DISCUSSION

The MUSE-ALMA Haloes survey has uncovered 79 galaxies associated with 32 H I Ly-α absorbers. These absorbers vary significantly in column density ($18 \lesssim \log[N({\rm H\,I})/{\rm cm}^{-2}] \lesssim 21.7$) and cover redshift $0.19 < z < 1.15$. The majority (17 out of 32) have two or more galaxies within ±500 kms^{-1} of the H I gas and only five absorbers do not have any associated galaxy detected in the MUSE data. In this section, we discuss the implications of our results on the distribution of gas and metals in the CGM and how galaxy properties, such as SFR and metallicity, correlate with absorber properties.

Table 3. Properties of the galaxy overdensities found at the absorber redshift. The number of expected galaxies for each absorber is calculated using the [O II] and [O III] luminosity functions (Comparat et al. 2016). We also include estimations of the group dispersion, $\sigma_{\rm group}$, and virialized group mass, but note these are lower limits because there may be galaxies outside the MUSE FoV. For the $z_{\rm abs} = 0.3929$ absorber towards Q1211 + 1030, the three associated galaxies have a maximum velocity separation of ∼25 kms^{-1} between them which results in the smaller $N_{\rm expected}$, $\sigma_{\rm group}$ and group mass measurements.

Quasar	$z_{\rm abs}$	$N_{\rm expected}$	$N_{\rm gal}$	$\sigma_{\rm group}$ (kms^{-1})	Group mass (log M$_\odot$)
Q0152 + 0023	0.4818	0.48	4	190	12.4
Q0152 − 2001	0.3830	0.40	5	100	12.3
Q0420 − 0127	0.6331	0.10	4	110	12.1
Q1110 + 0048	0.5604	0.04	3	100	12.0
Q1130 − 1449	0.3130	0.18	13	120	11.8
Q1211 + 1030	0.3929	0.002	3	13	10.0
Q1211 + 1030	0.8999	2.0	3	190	12.9
Q1229 − 021	0.7691	0.07	3	150	12.3
Q1229 − 021	0.8311	0.28	4	67	12.4
Q1515 + 0410	0.5592	0.07	4	22	11.1
Q2131 − 1207	0.4298	0.12	4	83	12.0

5.1 Number counts of galaxies associated with H I absorbers

5.1.1 Galaxy overdensities

Galaxy overdensities are increasingly being found at the redshift of absorbers. Compiling our results with surveys, such as CUBS (Chen et al. 2020a) and BASIC (Berg et al. 2022), we find that out of the 48 total absorbers with MUSE data, ∼50 per cent (23/48) are associated with two or more galaxies. There are eight non-detections of galaxies within the vicinity of absorbers and 30 per cent (16/48) have only one associated galaxy. We note that these IFS studies vary significantly in depth (∼3 mag in the *r*-band), and it is likely that the proportion of H I absorbers associated with two or more galaxies is higher in reality than indicated by the combined results of these surveys. Moreover, the number of associated galaxies also depends on the selection criteria. For the values given above, we count galaxies within ±500 kms^{-1} of the absorber to be associated but emphasize that stricter criteria will alter the results.

For all absorbers with >2 galaxies within 500 kms^{-1} of the absorber redshift, we compute the expected number of galaxies within a co-moving volume using the [O II] and [O III] luminosity functions scaled by z from Comparat et al. (2016; the latter only when [O II] flux measurements are unavailable). We assume a cylindrical volume with diameter equal to the largest separation between associated galaxies and height equal to the co-moving distance between the minimum and maximum associated galaxy redshifts. The number of galaxies found are on order 10^1–10^3 larger compared to the expected number (see Table 3). Importantly, the high $N_{\rm H\,I}$ values of the absorbers means that we know *a priori* that there is likely a galaxy at the absorber redshift. Our calculations of the expected number of galaxies using a luminosity function does not take this into account.

We also estimate group masses for all absorbers with more than three associated galaxies and these values are tabulated in Table 3. A *gapper* function (Beers, Flynn & Gebhardt 1990) is used to determine the velocity dispersion $\sigma_{\rm group}$ between group members and the virial theorem is applied ($M_{\rm group} \sim 3R\sigma^2_{\rm group}/G$), assuming the radius R is half the largest separation between galaxies in the field. We emphasize this estimate is a lower limit because many systems likely contain objects outside the MUSE FoV.

5.1.2 Absorbers without associated galaxies

We find that for five absorbers, there are no galaxies found within 500 kms^{-1} of the absorber redshift. There are three possible causes for this: (i) the absence of galaxy counterparts is due to an intrinsic property of the absorber such as H I column density or metallicity, (ii) there are galaxies outside the MUSE FoV, or (iii) there are galaxies below our detection limits.

The absorbers with missing galaxy counterparts span column densities of $\log[N({\rm H\,I})/{\rm cm}^{-2}] = 18.62$–$21.54$. Additionally, three out of the five absorbers have measured [Zn/H] abundances of -0.92, -0.45, and 0.08. Berg et al. (2022) found the population of pLLS and LLS systems to be bimodal and metal-poor absorbers (abundances [X/H] ≤ -1) not associated with any galaxies. The work suggests a population of $\log[N({\rm H\,I})/{\rm cm}^{-2}]<17.0$ absorbers may trace gas associated with overdense regions of the Universe rather than galaxy haloes. In the MUSE-ALMA Haloes survey, the higher column density of the absorbers studied means the gas is more likely found in galaxy haloes rather than these purported overdense regions. The metal abundances of the absorbers without galaxy counterparts are also enhanced compared to the values found in Berg et al. (2022).

Another possibility is that there are galaxies outside the MUSE FoV. The lowest redshift absorber without an associated galaxy is towards Q2353 − 0028 at $z_{\rm abs} = 0.6044$ where 30 arcsec corresponds to >200 kpc. In the MUSE-ALMA Haloes sample, ∼95 per cent of associated galaxies are found within 200 kpc, which indicates the missing galaxy counterparts are likely not beyond the FoV. Expanding our search to $|\Delta v| \leq 3000$ kms^{-1} reveals only one galaxy with velocity difference -2685.2 kms^{-1} for the absorber towards Q2353 − 0028. However, the extreme column density ($\log[N({\rm H\,I})/{\rm cm}^{-2}] = 21.54$) of this system suggests the host galaxy is within a few kpc (< 1 arcsec) of the absorber (Noterdaeme et al. 2014). Hence, the associated galaxy may be a passive dwarf galaxy within the PSF of the QSO. In fact, there are two more absorbers (Q0058 + 0019 at $z_{\rm abs} = 0.6127$ and Q0123 − 0058 at $z_{\rm abs} = 1.4094$) with column densities $\log[N({\rm H\,I})/{\rm cm}^{-2}] > 20$ and no galaxy counterpart. The results in the left-hand panel of Fig. 7 suggest the associated galaxy should be within 20 kpc of the QSO sightline and this is consistent with the characteristic sub-damped Ly-α (DLA) radius (Péroux et al. 2005).

While there are no associated galaxies detected in the MUSE data, the HST imaging after QSO subtraction reveals faint >25 mag objects within several arcseconds of the quasar for the Q0058 + 0019, Q1211 + 1030, and Q2353 − 0028 fields. These are candidate galaxy counterparts to the absorbers but no emission lines were detected at their positions in the MUSE data. Thus, the absorbers without confirmed associated galaxy detections in the MUSE data may have a nearby, passive galaxy. There is no HST imaging for the Q0123 − 0058 field so we could not search for galaxies near the QSO. The complete set of full and QSO-subtracted HST images will be presented in Karki et al. (in preparation).

Recent works studying the properties of absorbers passing within ∼50 kpc of quiescent galaxies have found enhanced N(Fe II)/N(Mg II) values compared to SF galaxies, suggested to arise from type 1a supernovae chemically enriching cool gas in the ISM and outer CGM (Zahedy et al. 2016, 2017; Boettcher et al. 2021). We note that here the insufficient depth in the MUSE data (particularly the Q0058 + 0019 and Q0123 − 0058 fields) and high redshift of absorbers limits the ability to detect galaxy counterparts, without necessarily indicating the galaxies associated with the absorbers would be passive. Indeed, Table 1 indicates that even SF galaxies will have emission fluxes below the detection limits in these data cubes. None the less, we compute N(Fe II)/N(Mg II) values for the absorbers for which the data are available. We find that Fe/Mg values of -0.5 and -0.26 (Pettini et al. 2000; Nielsen et al. 2016) for two un-detected absorbers with measured ion column densities (Q0058 + 0019 at $z_{\rm abs} = 0.6127$ and Q1211 + 1030 at $z_{\rm abs} = 1.05$, respectively) are comparable to the values of Fe/Mg $=-0.23$ and -0.75 (Muzahid et al. 2016; Pointon et al. 2019) for the sample of galaxies with detected associated galaxies. We will expand on this interesting point when more absorption metallicity measurements become available.

The large span in the intrinsic properties of the absorbers without galaxy counterparts and the large MUSE FoV compared to the expected location of associated galaxies signify that there are likely galaxies below the detection limit of the MUSE observations. Indeed, three of the five absorbers without galaxy detections belong to the fields with the worst seeing conditions (seeing FWHM = 1.23 for Q0058 + 0019 and 2.11 for Q0123 − 0058). The magnitude limit is likewise poorer than in other fields, and there are likely galaxies with SDSS r-band magnitudes >24 not detected by MUSE. The final absorber without a galaxy counterpart is towards QSO J1211 + 1030 at $z_{\rm abs} = 1.0496$. At this redshift, a main-sequence galaxy with SFR $\log({\rm SFR}) < 8.9$ M$_\odot$ yr^{-1} would not be detected. We conclude that our non-detections of associated galaxies are most likely caused by insufficient depth in the observations.

5.2 Star formation rates and BPT diagram

In the right-hand panel of Fig. 9, we find that the SFR appears to be higher for the most probable host galaxies at larger impact parameters. We plot in Fig. 14 the average SFR of all associated galaxies in bins of the velocity difference to the absorber ($|\Delta v|$) and impact parameter b. The bins have been artificially constructed such that there are approximately 10 galaxies in each bin. There appears to be no trend in the SFR as we approach larger $|\Delta v|$ and b bins.

From the [O III]/H β versus [O II]/H β diagram in Fig. 13, we find that the majority of galaxies (16/27) fall within the SF region. The expected percentage of AGNs at the median redshift of this sample $z \sim 0.39$ in galaxies with stellar mass $\log M_* = 10.1$ is 0.5 per cent (Aird, Coil & Georgakakis 2018). We use the median M_* of this sample, but note that this fraction is limited to AGN with specific black hole accretion rates >0.01 (the rate of black hole accretion normalized by the galaxy stellar mass). The median stellar mass for this flux-limited sample of galaxies is also higher than the larger population of associated galaxies in the MUSE-ALMA Haloes survey. Hence, while we find a larger fraction of AGN in our sample of associated galaxies (20 per cent of galaxies lie in the Seyfert 2 and LINER regions of the diagram) than normal, it remains unclear whether galaxies associated with H I absorbers are more likely to host AGN.

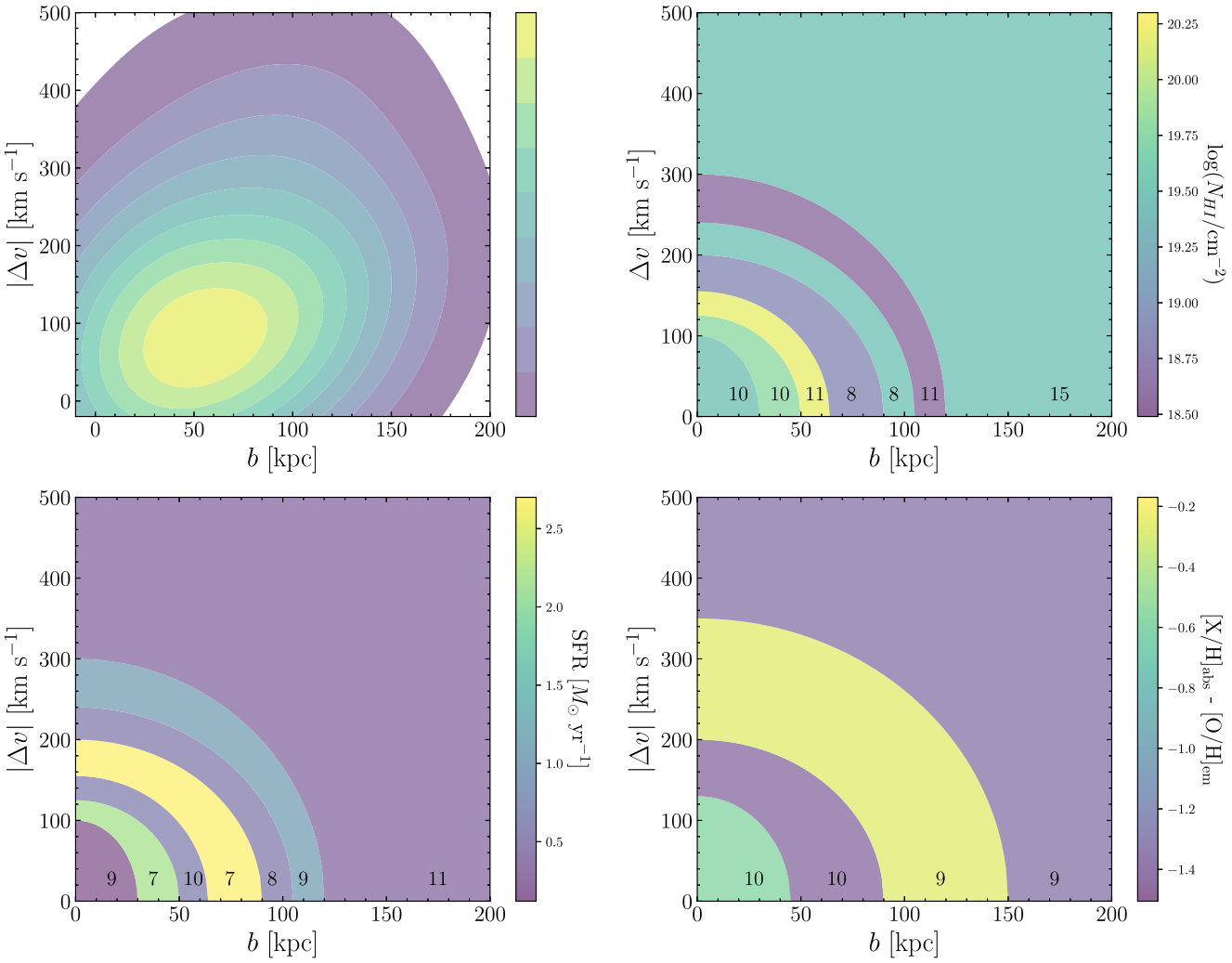

Figure 14. Median properties of galaxies and absorbers from the MUSE-ALMA Haloes survey at varying impact parameters and velocities. The distribution of gas and metals in the CGM can be mapped by a sufficiently large sample of QSO-galaxy pairs. The radial bins are distributed such that there are ∼10 galaxies in each bin (see labels within each bin for the exact value). Velocity and impact parameter in the plots extents are artificial and caused by forcing associated galaxies to be within ±500 kms^{-1}. Each bin is coloured by the median value of the property being plotted. Top left: An absorber-centric smoothed kernel density estimation of galaxy number density with respect to the absorber. The majority of galaxies are located within 100 kpc and 100 kms^{-1} of the absorber (warmer colours represent regions of higher density). Top right: a galaxy-centric view of the median absorber H I column density at varying $|\Delta v|$ and b. We find a decrease in the column density towards higher velocities and impact parameters. Bottom left: The median SFR of galaxies as a function of $|\Delta v|$ and b. Galaxies near the absorber appear to have larger SFRs than those located further away, but the trend is not consistent across the bins. Bottom right: The median emission-line metallicity of galaxies as a function of $|\Delta v|$ and b. There appears to be no trend in Z_{gal} with increasing velocity difference or impact parameter.

5.3 Distribution of gas in the CGM

We see in H I 21-cm emission maps of galaxies in the local Universe that the H I column density decreases with radius until the ionizing radiation field causes a sharp truncation (Maloney 1993; Zwaan et al. 2005). Extending beyond the neutral gas disc to the CGM, similar trends have been found where log N(H I) decreases as impact parameter increases (e.g. Lehner et al. 2013; Tumlinson et al. 2013; Prochaska et al. 2017). The range of neutral gas column densities often spans ∼3 dex for a given impact parameter, although it is important to acknowledge that part of this observation may be attributed to the galaxy-to-galaxy variation within the associated galaxy sample. Nevertheless, the scatter is significant enough that it indicates the CGM is 'clumpy' and the possible reasons for this are manifold. Recent work using high-redshift lensed quasars or galaxies as a background source show variations in the H I column density of up to 1 dex in physical separations of only 2–9 kpc (Kulkarni et al. 2019; Lopez et al. 2020; Cashman et al. 2021; Bordoloi et al. 2022, and references therein). A factor of 5 difference in optical depths is even found on parsec scales using 21-cm absorption towards compact symmetric objects (Biggs et al. 2016). Combining observations towards a quadruply lensed quasar with simulations, Augustin et al. (2021) finds fractional variations in Mg II EW are dependent on the underlying structure probed by the absorber. While outflows are found to be 'clumpy', inflowing filaments have smaller variations in EW. Recent gravitational-arc tomography of a galaxy at $z = 0.77$ also finds large variations in Mg II EW in a galaxy's extended rotating disc (Tejos et al. 2021). These studies reveal the CGM may be intrinsically clumpy, leading to the broad range of column densities observed at all impact parameters.

Moreover, ∼50 per cent of the absorbers are associated with more than one galaxy. While our criteria likely select the host of the H I

absorber, they do not account for situations where the gas is tidally stripped or part of the IGrM. The view of a one-to-one correlation between the absorber and the associated galaxy may contribute to the scatter seen in the relationship between $\log N(\mathrm{H\,I})$ and impact parameter. It is clear that neutral gas in the CGM does not follow a homogeneous and uniformly decreasing distribution out to larger radii. Despite this, our observations still indicate that lower column density gas is found further away from the galaxy centre, extending the trend seen in H I 21-cm maps of local galaxies (e.g. Elagali et al. 2019; Kleiner et al. 2019) to the CGM.

We plot in the top right of Fig. 14 the median column density of absorbers found at different velocities and impact parameters from the associated galaxy. The plot can be interpreted as being 'galaxy-centric'; the galaxy is at the origin and absorbers are placed afield. We find that galaxies associated with lower column density systems are typically found at larger velocities and impact parameters to the absorber. To test the impact of bin selection on this trend, we choose varying bin sizes in Fig. C1. Additionally, we also exclude the 13 galaxies associated with the $z_{\rm abs} = 0.313$ absorber towards Q1130 − 1449 to test whether removing this large galaxy group has a measurable impact on our results (Fig. C2). For these cases, we still find that the H I column density decreases at larger $|\Delta v|$ and b values.

While a clear anticorrelation between $\log N(\mathrm{H\,I})$ and impact parameter is seen in Fig. 7, there is no equivalent trend when plotting the column density against the velocity difference (Fig. 8). Thus, it becomes important to check whether the change in H I column density is primarily dictated by the impact parameter. We randomly shuffle the velocity differences between each associated galaxy and absorber, and find that $|\Delta v|$ plays little role in the changing column density (see Fig. C3). In contrast, randomly shuffling b produces a plot with little variation in H I column density across the bins (Fig. C4).

Finally, we respectively normalize both $|\Delta v|$ and impact parameter by the escape velocity and virial radius of each associated galaxy in Fig. C5. Details on this calculation are provided in Appendix C. Again, the column density decreases at larger virial radii, but the trend continues until $|\Delta v|/v_{\rm esc} \approx 1$ and $b/R_{\rm vir} \approx 3$. This suggests that neutral gas at velocities beyond the escape speed and distances several times the virial radius may no longer be associated with a galaxy. Overall, these results suggest that while the CGM may be inhomogeneous on scales less than several kpc, a statistical study can still reveal the broader change in the column density out to larger radii.

5.4 Distribution of metals in the CGM

Metallicity gradients can be found in studies of galaxy interstellar media in the local Universe (e.g. Sánchez et al. 2014; Belfiore et al. 2017) and at higher redshift (e.g. Carton et al. 2018; Curti et al. 2020b). The traditional inside-out growth model of galaxy formation suggests metallicity gradients will be negative, that is, the inner parts of the galaxy are more chemically enriched than the outer parts (Portinari & Chiosi 1999). However, physical processes such as outflows, inflows, and mergers will affect the gradient, flattening it out (Kewley et al. 2010; Bresolin, Kennicutt & Ryan-Weber 2012) or even inverting it (Sánchez Almeida et al. 2018). Further, moving from this 'inner' metallicity gradient to a gradient in the CGM presents a further challenge (e.g. Péroux et al. 2012; Christensen et al. 2014; Péroux et al. 2016; Rhodin et al. 2018; Kacprzak et al. 2019; Kulkarni et al. 2019).

Simulations from both EAGLE and TNG50 predict that despite the complexity of the physical processes of gas recycling (accretion, ejection, and reaccretion) and multiple origin along the los, the net metallicity of CGM gas is found to be higher along the minor axis because of outflows (Péroux et al. 2020). van de Voort et al. (2021) reach the same result using Auriga zoom-in simulations of a Milky Way-mass galaxy, but note that the introduction of magnetic fields decreases the mixing efficiency of inflowing and outflowing gas and subsequently increases the scatter in metallicities seen at a given azimuthal angle. While recent work from the MEGAFLOW survey suggests that gas along the minor axis is more dust-depleted and metal-enriched than the gas along the major axis (Wendt et al. 2021), a larger sample is required to observationally constrain the relationship between metallicity and azimuthal angle and account for the inherent inhomogeneity of the CGM (Zahedy et al. 2019, 2021; Bordoloi et al. 2022; Sameer et al. 2022). Despite these effects causing the metallicity to vary on small scales, predictions of a global trend in metallicity versus azimuthal angle are yet to be fully tested.

In Fig. 11, We find that >90 per cent of galaxies have confirmed emission-line metallicities larger than that of the absorbers. Fig. 12 reveals that the difference between the gas-phase metallicity measured via absorption and emission lines ($[\mathrm{X/H}]_{\rm abs} - [\mathrm{O/H}]_{\rm em}$) appears to increase in magnitude at higher impact parameters. However, the data required to constrain the relationship is currently too limited at $b > 40$ kpc to test whether the negative gradient found in previous studies extends to larger impact parameters (Chen et al. 2005; Christensen et al. 2014; Péroux et al. 2014). In the bottom-right panel of Fig. 14, we colour the radial bins by the median value of $[\mathrm{X/H}]_{\rm abs} - [\mathrm{O/H}]_{\rm em}$. We also include the sample of galaxies from the BASIC survey (Berg et al. 2022) with available galaxy and absorber metallicities. There appears to be a decrease in the metallicity from the first two radial bins (same trend seen with different binning in Appendix ref). Beyond the first two bins, the metallicity difference between absorber and galaxy begins to fluctuate. Part of the explanation for this is the fact that gas at these larger $|\Delta v|$ and b are beyond the virial radius of the galaxy and we expect the trend to no longer persist. More significantly, one must be cautious when comparing $[\mathrm{X/H}]_{\rm abs}$ with $[\mathrm{O/H}]_{\rm em}$. The former is a Zn or Fe abundance of the neutral phase in a gas cloud likely ∼100 pc in size while the oxygen abundance estimated from strong-line calibrations is an average ISM metallicity of the ionized gas. Factors such as alpha-element enhancements and varying calibrations of the measurements means that there are large systematic uncertainties when comparing the two metallicity measurements. However, given the diffuse nature of the CGM, gradients in the metallicity can only be studied thus far using a combination of emission and absorption.

6 SUMMARY AND CONCLUSION

We have analysed the physical and emission-line properties of 79 galaxies associated with 32 H I absorbers at redshift $0.20 \lesssim z \lesssim 1.4$. These associated galaxies are found at impact parameters ranging from 5.7 to 270 kpc and velocities −280 to +448 $\mathrm{kms^{-1}}$ relative to the absorber redshift. In the sample, there are passive galaxies without detectable emission lines and SF galaxies with SFRs up to 15 $\mathrm{M_\odot\,yr^{-1}}$. The emission-line metallicity of associated galaxies also varies from $12 + \log(\mathrm{O/H}) = 7.62$ to 8.75. When comparing the properties of associated galaxies with the absorber properties, we find:

(i) 27 out of the 32 absorbers have galaxy counterparts within ±500 $\mathrm{kms^{-1}}$. Out of these 27 absorbers, 18 (67 per cent) have two

or more associated galaxies and probe overdensities 1–3 dex larger than the expected number of galaxies within a co-moving volume at $z_{\rm abs}$. However, we note that the non-detections are likely caused by insufficient depth in the MUSE observations for the set of absorbers in the MUSE-ALMA Haloes sample and the detection rate is a strict lower limit.

(ii) By including results from SINFONI studies of galaxy counterparts to DLA systems, the BASIC and the CUBS, we find that the H I column density of absorbers is found to be anticorrelated with the impact parameter b of the nearest associated galaxy out to 120 pkpc. This relationship persists when we scale b by the virial radius of the most probable host galaxy. These results broadly agree with simulations of the CGM, and we find a >3 dex scatter in column density at any given impact parameter. The scatter highlights the intrinsic 'clumpiness' of CGM gas and that absorbers are often not associated with a single galaxy halo. However, the fact that a trend in $N_{\rm H\,I}(b)$ can be seen suggests large statistical studies can still reproduce the distribution of gas in the CGM.

(iii) A comparison of the emission metallicity from the ISM of associated galaxies and absorber metal abundance reveals the neutral gas phase in the CGM is lower metallicity than the ISM. From the limited absorber metallicity measurements, there appears to be a negative gradient in the CGM metallicity as we go to larger values of b and Δv. However, this result is limited by the complications that come with comparing metallicity measurements of two distinct gas phases and elements.

(iv) Adopting a galaxy-centric view and plotting absorbers in velocity difference and impact parameter space indicates that the column density of gas decreases at large values of b and $|\Delta v|$. However, we find this is largely driven by the anticorrelation between $N_{\rm H\,I}$ and b. There appears to be no trend between the H I column density and the velocity difference between associated galaxy and absorber. This is caused by the uncertainty in the origin of the absorber, that is, whether the neutral gas is found to be co-rotating with the galaxy disc, outflowing or accreting onto the galaxy. Future works will seek to determine the origins of the gas and more deeply relate the absorber properties with the host of the absorber.

The analysis of the 19 MUSE fields from the MUSE-ALMA Haloes survey highlight that the increasing number of absorber–galaxy pairs allows for a statistical study of how the gas and metals are distributed in the CGM. For the absorbers without associated galaxies, we emphasize the need for deeper observations to improve the completeness of the sample and to follow-up candidate-associated galaxies at small b seen in the HST imaging. Additionally, higher spatial resolution data of the region near the QSO is essential to uncover passive galaxies that may be responsible for the absorber. In future, surveys such as the 4MOST (de Jong et al. 2012; de Jong et al. 2019) H I-Q survey (PI: C. Péroux) will seek to increase the number of absorber-galaxy pairs by several orders of magnitude. The 2.8 Million fiber hour-survey will observe over one million background quasars with spectral resolution $R = 20\,000$ in fields with deep observations of foreground objects (galaxies, AGNs, and clusters). Ultimately, these massive statistical samples will allow us to map the gas and metal distribution of the CGM.

ACKNOWLEDGEMENTS

This research is supported by an Australian Government Research Training Program (RTP) Scholarship. EMS, GK, and SW acknowledge the financial support of the Australian Research Council through grant CE170100013 (ASTRO3D). VPK and AK acknowledge partial support for GO program 15939 (PI: Peroux) provided through a grant from the STScI under NASA contract NAS5-26555 and NASA grant 80NSSC20K0887 (PI: Kulkarni). VPK also gratefully acknowledges additional support from the National Science Foundation grants AST/2007538 and AST/2009811 (PI: Kulkarni). We thank the International Space Science Institute (ISSI; https://www.issibern.ch/) for financial support.

We thank Thomas Ott for developing and distributing the QFITSVIEW software. This research also made use of several PYTHON packages: ASTROPY (Astropy Collaboration 2013, 2018), MATPLOTLIB (Hunter 2007), NUMPY (Harris et al. 2020), and SCIPY (Virtanen et al. 2020).

DATA AVAILABILITY

Data directly related to this publication and its figures are available upon request. The raw data can be downloaded from the public archives with the respective project codes.

REFERENCES

Aird J., Coil A. L., Georgakakis A., 2018, MNRAS, 474, 1225
Asplund M., Grevesse N., Sauval A. J., Scott P., 2009, ARA&A, 47, 481
Astropy Collaboration, 2013, A&A, 558, A33
Astropy Collaboration, 2018, AJ, 156, 123
Augustin R. et al., 2018, MNRAS, 478, 3120
Augustin R., Péroux C., Hamanowicz A., Kulkarni V., Rahmani H., Zanella A., 2021, MNRAS, 505, 6195
Bacon R. et al., 2010, in McLean I. S., Ramsay S. K., Takami H., eds, Proc. SPIE Conf. Ser., Vol. 7735, Ground-based and Airborne Instrumentation for Astronomy III. SPIE, Bellingham, p. 773508
Bacon R., Piqueras L., Conseil S., Richard J., Shepherd M., 2016, Astrophysics Source Code Library, record ascl:1611.003
Baldwin J. A., Phillips M. M., Terlevich R., 1981, PASP, 93, 5
Beers T. C., Flynn K., Gebhardt K., 1990, AJ, 100, 32
Belfiore F. et al., 2017, MNRAS, 469, 151
Berg T. A. M., Ellison S. L., Tumlinson J., Oppenheimer B. D., Horton R., Bordoloi R., Schaye J., 2018, MNRAS, 478, 3890
Berg M. A. et al., 2022, preprint (arXiv:2204.13229)
Bergeron J., 1986a, A&A, 155, L8
Bergeron J., 1986b, A&A, 155, L8
Bergeron J., Boissé P., 1991, A&A, 243, 344
Biggs A. D., Zwaan M. A., Hatziminaoglou E., Péroux C., Liske J., 2016, MNRAS, 462, 2819
Boettcher E. et al., 2021, ApJ, 913, 18
Boisse P., Le Brun V., Bergeron J., Deharveng J.-M., 1998, A&A, 333 , 841
Bordoloi R. et al., 2022, Nature, 606, 59
Borthakur S. et al., 2015, ApJ, 813, 46
Bouché N., Murphy M. T., Péroux C., Davies R., Eisenhauer F., Förster Schreiber N. M., Tacconi L., 2007, ApJ, 669, L5
Bouché N., Murphy M. T., Kacprzak G. G., Péroux C., Contini T., Martin C. L., Dessauges-Zavadsky M., 2013, Science, 341, 50
Bresolin F., Kennicutt R. C., Ryan-Weber E., 2012, ApJ, 750, 122
Burchett J. N., Rubin K. H. R., Prochaska J. X., Coil A. L., Vaught R. R., Hennawi J. F., 2021, ApJ, 909, 151
Cameron A. J. et al., 2021, ApJ, 918, L16
Carton D. et al., 2018, MNRAS, 478, 4293
Cashman F. H., Kulkarni V. P., Lopez S., 2021, AJ, 161, 90
Chabrier G., 2003, PASP, 115, 763
Chen Y. et al., 2020b, MNRAS, 499, 1721
Chen H.-W., Mulchaey J. S., 2009, ApJ, 701, 1219
Chen H.-W., Kennicutt R. C. Jr., Robert C. J., Rauch M., 2005, ApJ, 620, 703
Chen H.-W., Zahedy F. S., Johnson S. D., Pierce R. M., Huang Y.-H., Weiner B. J., Gauthier J.-R., 2018, MNRAS, 479, 2547

Chen H.-W., Boettcher E., Johnson S. D., Zahedy F. S., Rudie G. C., Cooksey K. L., Rauch M., Mulchaey J. S., 2019, ApJ, 878, L33
Chen H.-W. et al., 2020a, MNRAS, 497, 498
Christensen L., Møller P., Fynbo J. P. U., Zafar T., 2014, MNRAS, 445, 225
Comparat J. et al., 2016, MNRAS, 461, 1076
Cooper T. J. et al., 2021, MNRAS, 508, 4359
Curti M., Cresci G., Mannucci F., Marconi A., Maiolino R., Esposito S., 2017, MNRAS, 465, 1384
Curti M., Mannucci F., Cresci G., Maiolino R., 2020a, MNRAS, 491, 944
Curti M. et al., 2020b, MNRAS, 492, 821
de Jong R. S. et al., 2012, in McLean I. S., Ramsay S. K., Takami H., eds, Proc. SPIE Conf. Ser., Vol. 8446, Ground-based and Airborne Instrumentation for Astronomy IV. SPIE, Bellingham, p. 84460T
de Jong R. S. et al., 2019, The Messenger, 175, 3
Dutta R. et al., 2020, MNRAS, 499, 5022
Elagali A. et al., 2019, MNRAS, 487, 2797
Epinat B. et al., 2018, A&A, 609, A40
Fraternali F., 2017, in Astrophysics and Space Science Library, Vol. 430, Gas Accretion onto Galaxies. p. 323
Gharanfoli S., Kulkarni V. P., Chun M. R., Takamiya M., 2007, AJ, 133, 130
Grand R. J. J. et al., 2017, MNRAS, 467, 179
Hamanowicz A. et al., 2020, MNRAS, 492, 2347
Harris C. R. et al., 2020, Nature, 585, 357
Helton J. M., Johnson S. D., Greene J. E., Chen H.-W., 2021, MNRAS, 505, 5497
Hinton S. R., Davis T. M., Lidman C., Glazebrook K., Lewis G. F., 2016, Astron. Comput., 15, 61
Ho S. H., Martin C. L., Schaye J., 2021, ApJ, 923, 137
Huang Y.-H., Chen H.-W., Shectman S. A., Johnson S. D., Zahedy F. S., Helsby J. E., Gauthier J.-R., Thompson I. B., 2021, MNRAS, 502, 4743
Hunter J. D., 2007, Comput. Sci. Eng., 9, 90
Jenkins E. B., 2009, ApJ, 700, 1299
Johnson S. D. et al., 2018, ApJ, 869, L1
Kacprzak G. G., Pointon S. K., Nielsen N. M., Churchill C. W., Muzahid S., Charlton J. C., 2019, ApJ, 886, 91
Kennicutt, Robert C. J., 1998, ApJ, 498, 541
Kewley L. J., Rupke D., Zahid H. J., Geller M. J., Barton E. J., 2010, ApJ, 721, L48
Kleiner D. et al., 2019, MNRAS, 488, 5352
Klitsch A., Péroux C., Zwaan M. A., Smail I., Oteo I., Biggs A. D., Popping G., Swinbank A. M., 2018, MNRAS, 475, 492
Kulkarni V. P., Cashman F. H., Lopez S., Ellison S. L., Som D., Maureira M. J., 2019, ApJ, 886, 83
Kulkarni V. P., Bowen D. V., Straka L. A., York D. G., Gupta N., Noterdaeme P., Srianand R., 2022, ApJ, 929, 150
Lamareille F., 2010, A&A, 509, A53
Leclercq F. et al., 2022, A&A. 663, A11
Lehner N. et al., 2013, ApJ, 770, 138
Liang C. J., Chen H.-W., 2014, MNRAS, 445, 2061
Lofthouse E. K. et al., 2020, MNRAS, 491, 2057
Lopez S. et al., 2020, MNRAS, 491, 4442
Maloney P., 1993, ApJ, 414, 41
Meiring J. D., Kulkarni V. P., Lauroesch J. T., Péroux C., Khare P., York D. G., 2009, MNRAS, 393, 1513
Momose R. et al., 2014, MNRAS, 442, 110
Morrissey P. et al., 2018, ApJ, 864, 93
Muzahid S., Kacprzak G. G., Charlton J. C., Churchill C. W., 2016, ApJ, 823, 66
Muzahid S. et al., 2020, MNRAS, 496, 1013
Navarro J. F., Frenk C. S., White S. D. M., 1997, ApJ, 490, 493
Nelson D. et al., 2020, MNRAS, 498, 2391
Nestor D. B., Pettini M., Hewett P. C., Rao S., Wild V., 2008, MNRAS, 390, 1670
Nielsen N. M., Churchill C. W., Kacprzak G. G., Murphy M. T., Evans J. L., 2016, ApJ, 818, 171
Nielsen N. M., Kacprzak G. G., Pointon S. K., Murphy M. T., Churchill C. W., Davé R., 2020, ApJ, 904, 164
Noterdaeme P., Petitjean P., Pâris I., Cai Z., Finley H., Ge J., Pieri M. M., York D. G., 2014, A&A, 566, A24
Osterbrock D. E., 1989, Astrophysics of gaseous nebulae and active galactic nuclei
Ott T., 2012, Astrophysics Source Code Library, record ascl:1210.019
Pei Y. C., 1992, ApJ, 395, 130
Péroux C., Howk J. C., 2020, ARA&A, 58, 363
Péroux C., Dessauges-Zavadsky M., D'Odorico S., Sun Kim T., McMahon R. G., 2005, MNRAS, 363, 479
Péroux C., Meiring J. D., Kulkarni V. P., Khare P., Lauroesch J. T., Vladilo G., York D. G., 2008, MNRAS, 386, 2209
Péroux C., Bouché N., Kulkarni V. P., York D. G., Vladilo G., 2012, MNRAS, 419, 3060
Péroux C., Bouché N., Kulkarni V. P., York D. G., 2013, MNRAS, 436, 2650
Péroux C., Kulkarni V. P., York D. G., 2014, MNRAS, 437, 3144
Péroux C. et al., 2016, MNRAS, 457, 903
Péroux C. et al., 2017, MNRAS, 464, 2053
Péroux C. et al., 2019, MNRAS, 485, 1595
Péroux C., Nelson D., van de Voort F., Pillepich A., Marinacci F., Vogelsberger M., Hernquist L., 2020, MNRAS, 499, 2462
Péroux C. et al., 2022, MNRAS, 516, 5618
Pettini M., Pagel B. E. J., 2004, MNRAS, 348, L59
Pettini M., Ellison S. L., Steidel C. C., Shapley A. E., Bowen D. V., 2000, ApJ, 532, 65
Pointon S. K., Kacprzak G. G., Nielsen N. M., Muzahid S., Murphy M. T., Churchill C. W., Charlton J. C., 2019, ApJ, 883, 78
Portinari L., Chiosi C., 1999, A&A, 350, 827
Prochaska J. X. et al., 2017, ApJ, 837, 169
Rafelski M., Wolfe A. M., Prochaska J. X., Neeleman M., Mendez A. J., 2012, ApJ, 755, 89
Rahmani H. et al., 2016, MNRAS, 463, 980
Rahmani H. et al., 2018a, MNRAS, 474, 254
Rahmani H. et al., 2018b, MNRAS, 480, 5046
Rao S. M., Turnshek D. A., Nestor D. B., 2006, ApJ, 636, 610
Rhodin N. H. P., Christensen L., Møller P., Zafar T., Fynbo J. P. U., 2018, A&A, 618, A129
Ribaudo J., Lehner N., Howk J. C., Werk J. K., Tripp T. M., Prochaska J. X., Meiring J. D., Tumlinson J., 2011, ApJ, 743, 207
Robotham A. S. G., Davies L. J. M., Driver S. P., Koushan S., Taranu D. S., Casura S., Liske J., 2018, MNRAS, 476, 3137
Rodríguez-Puebla A., Primack J. R., Avila-Reese V., Faber S. M., 2017, MNRAS, 470, 651
Salpeter E. E., 1955, ApJ, 121, 161
Sameer et al., 2022, MNRAS, 510, 5796
Sánchez Almeida J., Caon N., Muñoz-Tuñón C., Filho M., Cerviño M., 2018, MNRAS, 476, 4765
Sánchez S. F. et al., 2014, A&A, 563, A49
Savage B. D., Sembach K. R., 1996, ARA&A, 34, 279
Schreiber C. et al., 2015, A&A, 575, A74
Schroetter I., Bouché N., Péroux C., Murphy M. T., Contini T., Finley H., 2015, ApJ, 804, 83
Schroetter I. et al., 2016a, ApJ, 833, 39
Schroetter I. et al., 2016b, ApJ, 833, 39
Shull J. M., 2014, ApJ, 784, 142
Spitzer L. J., Jenkins E. B., 1975, ARA&A, 13, 133
Steidel C. C., Bogosavljević M., Shapley A. E., Kollmeier J. A., Reddy N. A., Erb D. K., Pettini M., 2011, ApJ, 736, 160
Szakacs R. et al., 2021, MNRAS, 505, 4746
Tejos N. et al., 2021, MNRAS, 507, 663
Thom C., Werk J. K., Tumlinson J., Prochaska J. X., Meiring J. D., Tripp T. M., Sembach K. R., 2011, ApJ, 736, 1
Tumlinson J. et al., 2013, ApJ, 777, 59
Tumlinson J., Peeples M. S., Werk J. K., 2017, ARA&A, 55, 389
van de Voort F., Springel V., Mandelker N., van den Bosch F. C., Pakmor R., 2019, MNRAS, 482, L85
van de Voort F., Bieri R., Pakmor R., Gómez F. A., Grand R. J. J., Marinacci F., 2021, MNRAS, 501, 4888

Virtanen P. et al., 2020, Nature Methods, 17, 261
Vladilo G., Abate C., Yin J., Cescutti G., Matteucci F., 2011, A&A, 530, A33
Wendt M., Bouché N. F., Zabl J., Schroetter I., Muzahid S., 2021, MNRAS, 502, 3733
York D. G. et al., 2006, MNRAS, 367, 945
Zabl J. et al., 2021, MNRAS, 507, 4294
Zahedy F. S., Chen H.-W., Rauch M., Wilson M. L., Zabludoff A., 2016, MNRAS, 458, 2423
Zahedy F. S., Chen H.-W., Gauthier J.-R., Rauch M., 2017, MNRAS, 466, 1071
Zahedy F. S., Chen H.-W., Johnson S. D., Pierce R. M., Rauch M., Huang Y.-H., Weiner B. J., Gauthier J.-R., 2019, MNRAS, 484, 2257
Zahedy F. S. et al., 2021, MNRAS, 506, 877
Zwaan M. A., van der Hulst J. M., Briggs F. H., Verheijen M. A. W., Ryan-Weber E. V., 2005, MNRAS, 364, 1467

Zych B. J., Murphy M. T., Pettini M., Hewett P. C., Ryan-Weber E. V., Ellison S. L., 2007, MNRAS, 379, 1409

SUPPORTING INFORMATION

Supplementary data are available at *MNRAS* online.

Table 2. Summary of associated galaxy properties.
Appendix A. Muse fields.
Appendix B. Varying selection criteria for the most probable galaxy host.
Appendix C. Changing H I column density with impact parameter and velocity difference to the absorber.

Please note: Oxford University Press is not responsible for the content or functionality of any supporting materials supplied by the authors. Any queries (other than missing material) should be directed to the corresponding author for the article.

This paper has been typeset from a TEX/LATEX file prepared by the author.